INTERNATIONAL JOURNAL FOR NUMERICAL METHODS IN FLUIDS, VOL. 7, 761–791 (1987)

PETROV–GALERKIN METHODS FOR NATURAL CONVECTION IN DIRECTIONAL SOLIDIFICATION OF BINARY ALLOYS

PETER M. ADORNATO AND ROBERT A. BROWN

Department of Chemical Engineering and Materials Processing Center, Massachusetts Institute of Technology, Cambridge, MA 02139, U.S.A.

SUMMARY

A Petrov–Galerkin finite element method is presented for calculation of the steady, axisymmetric thermosolutal convection and interface morphology in a model for vertical Bridgman crystal growth of non-dilute binary alloys. The Petrov–Galerkin method is based on the formulation for biquadratic elements developed by Heinrich and Zienkiewicz and is introduced into the calculation of the velocity, temperature and concentration fields. The algebraic system is solved simultaneously for the field variables and interface shape by Newton's method. The results of the Petrov–Galerkin method are compared critically with those of Galerkin's method using the same finite element grids. Significant improvements in accuracy are found with the Petrov–Galerkin method only when the mesh is refined and when the formulation of the residual equations is modified to account for the mixed boundary conditions that arise at the solidification interface. Calculations for alloys with stable and unstable solute gradients show the occurrence of classical flow transitions and morphological instabilities in the solidification system.

KEY WORDS Convection–Diffusion Problems Petrov–Galerkin Methods Free-Boundary Problems Solidification

1. INTRODUCTION

The interest in describing convection in the melt near a solidifying solid has intensified in recent years with the increasing focus on detailed understanding of the role of transport processes in setting the quality of bulk metals and semiconductors grown from the melt.[1,2] In many solidification processes buoyancy-driven or thermosolutal convection caused by non-uniformities in the temperature and concentration fields interact with heat and solute transport and the morphology of the melt/solid interface to affect adversely the compositional uniformity and the crystalline quality of the product solid. Detailed analysis for optimization of the design and control of crystal growth systems requires efficient and accurate numerical methods for the complex free- and moving-boundary problems that describe solidification including thermosolutal convection.

In previous reports[3–5] we have described a Galerkin finite element analysis coupled with a Newton iteration procedure for simultaneous calculation of the field variables and interface shape for steady-state solidification problems. These analyses used standard isoparametric mixed finite element representations of the velocity, pressure, temperature and solute fields and a consistent polynomial approximation to the melt/solid interface. Galerkin's method was employed to reduce the partial differential equations to a non-linear algebraic set and Newton's method coupled with direct Gaussian elimination was used to solve this set. The efficiency of the Newton scheme over more conventional methods that iterate sequentially between the field variables and interface

0271–2091/87/080761–31$15.50

Received 17 June 1986
Revised 19 November 1986

shape was demonstrated by Chang and Brown.[3] Besides yielding more rapid convergence to solutions of the discrete equation set, Newton's method is also the basis for computer-implemented perturbation methods for detecting multiple solutions, for tracking solutions in parameter space, and for determining solution stability with respect to small perturbations.[6] Chang and Brown[4] have used these features in conjunction with the finite element/Newton method for solving coupled convection–solidification problems for an idealized solidification problem.

Calculations that described the convection and solute transport processes in a laboratory-scale directional solidification system[5] uncovered a primary difficulty with the Galerkin approach. These calculations showed, and experiments have confirmed,[7] that intense laminar convection is present in these systems, so that a successful numerical simulation must resolve the resulting boundary layers in the velocity, temperature and solute fields. It is well known[8] that conventional Galerkin finite element approximations become numerically unstable for convection-dominated transport problems when the approximations do not adequately resolve the steep gradients in field variables. As a result, spurious oscillations with the spatial frequency of the mesh appear throughout the solution and destroy its usefulness.

Although the resolution of the Galerkin approximation can be improved and the oscillations removed by mesh refinement, this cure is impractical in many applications. The extremely fine meshes that are needed to resolve the field variables adequately enough to stabilize the Galerkin approximation for complicated two- and three-dimensional flow problems are not practical using present supercomputers, especially in the context of the Newton algorithm, which requires solution of large sets of linear equations. The convection–solidification problems addressed in this paper fall into this category. Here the difficulties with resolution of boundary and internal layers in the various field variables are aggravated by the disparities in the diffusivities for heat, species and momentum; characteristic values for these parameters are given in section 2.

The use of Petrov–Galerkin or 'upstream weighting' methods to alleviate the oscillations in under-refined Galerkin or centred-difference schemes is documented in the literature, as are the criticisms[8,9] inherent to any of these methods that purposely introduce artificial diffusivity into the approximation. Adaptive grid refinement is another alternative, but is complicated by the need for varying approximations for field variables with widely different diffusivities, which are dominant in the thermosolutal convection. The Petrov–Galerkin technique discussed here can be thought of as an attempt at constructing an adaptive formulation, which enhances the computation of convectively dominated equations when used in conjunction with adaptive refinement on a single mesh designed to aid resolution of boundary layers in all variables.

Finite element techniques for solving convectively dominated problems can be classified according to the formalism used to introduce artificial diffusivity into the Galerkin formulation. Methods based on modification of the numerical quadrature,[10] on direct introduction of an artificial diffusivity[11,12] and on modification of the weighting function in the weighted residual method (the Petrov–Galerkin method[13–15]) have all been proposed. From these methods we have chosen to use a particular Petrov–Galerkin formulation based on the adaptability of the method to two-dimensional problems on irregular grids, and the ease of the formulation of the method for higher-order, finite element basis functions. We have implemented the Petrov–Galerkin method proposed by Heinrich and Zienkiewicz[14] for Lagrangian biquadratic basis functions in our development of the conservation equations arising in the solidification problem. These authors have proposed to weight the residual equations with a sum of the conventional basis functions and an additional function chosen to solve exactly the one-dimensional convection–diffusion problem with essential boundary conditions, and generalized the formulation to problems in two space dimensions approximated by the eight-node quadratic and biquadratic isoparametric elements. We apply this method for the two-dimensional, biquadratic isoparametric elements and include

the more complicated mixed boundary conditions that arise in solidification problems. Heinrich[16] has implemented this Petrov–Galerkin formulation for bilinear elements in a transient analysis of thermosolutal convection. In this calculation, Heinrich omitted the Petrov–Galerkin weighting from the source terms arising from the coupling of the temperature and solute fields to the buoyancy force in the momentum balance, contending that adding this dependence led to erroneous results. We apply the Petrov–Galerkin formulation to all terms in the conservation equations.

In this paper we describe results from the combination of the Petrov–Galerkin method applied to each of the conservation equations for thermosolutal convection with the Newton iteration scheme presented previously for solution of steady-state solidification problems. This formulation is described in section 3. In section 4, the Petrov–Galerkin formulation is evaluated critically relative to the Galerkin method for the problem describing the solidification of a dilute binary alloy in the vertical Bridgman crystal growth geometry. This application is a fair test of the robustness of the algorithm, because it demands both flexibility of the formulation for approximating the mixed boundary conditions needed to describe transport across the solidification interface and accuracy of the approximation for capturing boundary and internal layers in the field variables.

The vertical Bridgman system is also a fertile ground for demonstrating the occurrence of well-known fluid mechanical instabilities caused by coupling of the temperature and solute fields and small scale morphological instabilities in the non-dilute system. Besides natural convection caused by the temperature gradients inherent in this system, gradients in the solute field during the solidification of a non-dilute alloy can also drive flow. Adding a heavier solute which is partitioned into the melt at the melt/solid interface should decrease the flow driven by radial temperature gradients by increasing the density of the melt in the diffusion-layer above the interface.

We also expect that a version of the sideways diffusive instability described by Hart[17] is possible. Hart showed that the parallel flow established between two vertical plates at different temperatures will become unstable in the presence of a constant axially stabilizing concentration gradient of sufficient magnitude. He showed that increasing the solute concentration (solutal Rayleigh number, Ra_s) at constant temperature difference (thermal Rayleigh number) caused a transition to a pattern of vertically layered flow cells. This transition appears as a steady-state bifurcation from the parallel-flow solution. The transient calculations of Heinrich[16] seem to indicate that stable cellular patterns are possible for Ra_s greater than the critical value. We expect that flow patterns like those described by Hart are possible in the solidification system, but that the non-uniformity of the thermal boundary conditions and the exponential variation of the solute concentration along the axis of the crystal will act as imperfections and break the bifurcation present in the idealized situation studied by Hart. We show this transition in section 5.1.

McFadden *et al.*[18] have studied solutally driven flows when the temperature field is vertically aligned and stabilizing and the solute profile corresponding to diffusion-controlled solidification lowers the melt density adjacent to the solidification interface. They have shown that thermosolutal convection begins at a critical solutal Rayleigh number and develops first as a cellular flow restricted to the region of melt containing the destabilizing solute gradient. As discussed by Chang and Brown,[4] laboratory furnaces have lateral temperature gradients that cause buoyancy-driven convection to exist for all non-zero temperature differences. These flows break the symmetry of the solute field in the case of a non-dilute alloy and lead to imperfect bifurcation from the diffusion-controlled state. This is demonstrated in section 5.2.

Adding the coupling of the melt/solid interface shape to the solute field through the dependence of the melting point on the local composition of the alloy makes it possible that local compositional supercooling of the melt will cause the transition from a locally planar to a cellular interface

morphology (spatial wavelength of the order of 100 μm). This transition has been rigorously examined without convection[19,20] and is another example of a bifurcation phenomenon that is ruptured by variations in the solute concentration along the interface, as demonstrated by Ungar and Brown.[21] We show in section 5.3 that solute variations caused by imperfect convective mixing can lead to cells that appear as mesh-dependent numerical instabilities in the convection–solidification problem. This coupling accentuates the difficulties with numerical simulation of complex non-linear phenomena that can manifest changes on drastically different length scales.

2. VERTICAL BRIDGMAN CRYSTAL GROWTH SYSTEM AND THERMOSOLUTAL CONVECTION

The idealized vertical Bridgman crystal growth considered here is shown in Figure 1. It consists of a cylindrical ampoule containing melt and solid that is translated through a furnace composed of hot and cold zones separated by an insulating region designed to cause planar isotherms near the melt/solid interface. Here we consider only the vertically stabilized Bridgman system where melt is placed above the solid and the radially averaged vertical temperature field is stabilizing with respect to buoyancy-driven convection. Then convection in a single-component melt is driven solely by radial temperature gradients caused by imperfections in the thermal boundary conditions. The unstable configuration with solid above a single-component melt was discussed by Chang and Brown.[4]

The motion of the ampoule and the growth of the crystal are modelled by uniform axial velocities through the top and bottom of the ampoule. This model corresponds to assuming that the ampoule extends far enough into both isothermal regions of the furnace that transients caused by the ends of the ampoule can be neglected. The growth rates in the melt V_m and solid V_s are related by the ratio of densities, $\sigma \equiv (\rho_s/\rho_m)$, as $V_m = \sigma V_s$. The concentration of the dilute component of the alloy

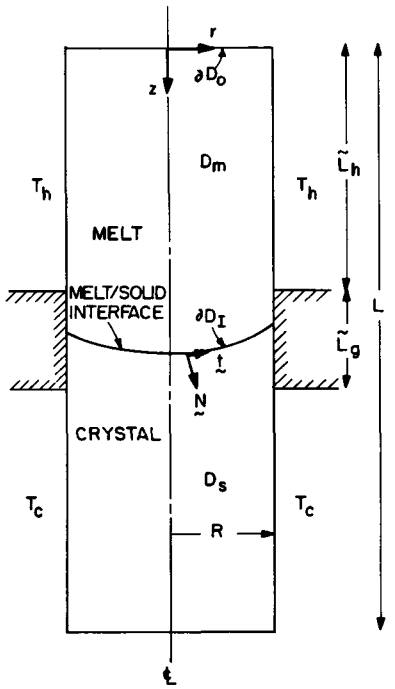

Figure 1. Schematic diagram of the stabilized vertical Bridgman crystal growth system

entering the ampoule is set to c_0, which is measured in mole per cent of the solute.

It is instructive to review the basic transport in diffusion controlled crystal growth in order to understand the driving forces for thermosolutal convection in the vertical Bridgman system. In the absence of thermosolutal convection and for a flat melt/solid interface, the profiles of temperature, solute concentration and fluid density have the shapes shown in Figure 2. The vertical temperature field will be linear (assuming that conduction dominates heat transport caused by the growth velocity V_m) with a discontinuity in slope at the interface caused by latent heat release and the change in thermal conductivities between the phases. For a single-component melt, the axial variation of the temperature field causes a decreasing density profile up from the interface, as long as there are no anomalies in the behaviour of the coefficient of thermal expansion with temperature and concentration.

Solute, which enters at the top of the ampoule, convects, downward at the growth velocity and is preferentially rejected ($k < 1$) or incorporated ($k > 1$) into the solid according to the thermodynamic segregation coefficient between solid and melt, $k \equiv c_s/c_m$, where the concentrations are evaluated at the interface. The resulting solute field has the well-known[22] exponential form shown in Figure 2. In a binary alloy, the axial variation of the melt density depends on the value of k and on the direction of the influence of increasing concentration on the density $\rho = \rho(c)$, so that the solute profile can have either a stabilizing or destabilizing effect on convection.

We consider the steady-state axisymmetric conservation equations for energy in the solid and melt, and for momentum, solute concentration, and continuity in the melt. Field variables are written in terms of a fixed cylindrical polar (r, θ, z) co-ordinate system with its origin at the top of the ampoule, and the height L of the ampoule is introduced as a length scale. The shape of the melt/solid interface is described by a single-valued function $z = h(r), 0 \leqslant r \leqslant \Lambda$, where $\Lambda \equiv R/L$ is the aspect ratio of the ampoule. The unit vectors normal $\mathbf{n}$ and tangent $\mathbf{t}$ of this surface are

$$\mathbf{n} \equiv (\mathbf{e}_z - h_r \mathbf{e}_r)/(1 + h_r^2)^{1/2}, \quad t \equiv (\mathbf{e}_r + h_r \mathbf{e}_z)/(1 + h_r^2)^{1/2}, \tag{1}$$

where $h_r \equiv \mathrm{d}h/\mathrm{d}r$. We define the dimensionless temperature and concentration fields as $\Theta(r, z) \equiv [T(r, z) - T_c]/(T_h - T_c)$ and $c \equiv \tilde{c}(r, z)/c_0$, respectively, where $T(r, z)$ and $\tilde{c}(r, z)$ are the dimensional fields and T_h and T_c are the temperatures of the hot and cold zones of the furnace.

The dimensionless conservation equations are written in terms of the reduced concentration field, $S(r, z) \equiv c(r, z) - 1$, as

$$\mathbf{v} \cdot \nabla \Theta = \nabla^2 \Theta, \tag{2}$$

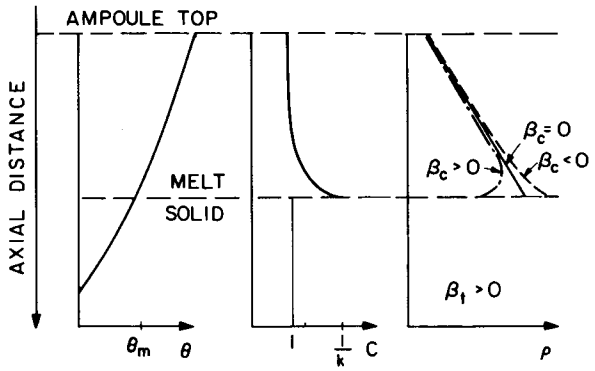

Figure 2. Axial dependence of the temperature, solute concentration and density profiles for a convectionless vertical Bridgman crystal growth system

$$(Sc/Pr)\mathbf{v}\cdot\nabla S = \nabla^2 S, \tag{3}$$

$$\mathbf{v}\cdot\nabla\mathbf{v} = -\nabla p + Pr\nabla^2\mathbf{v} + Pr[Ra_s S - Ra_t(\Theta - 1)], \tag{4}$$

$$\nabla\cdot\mathbf{v} = 0, \tag{5}$$

where ∇ is the gradient operator in cylindrical co-ordinates. The dimensionless velocity $\mathbf{v}(r, z)$ and pressure $p(r, z)$ fields are scaled with α_m/L and $\rho_m\alpha_m^2/L^2$, respectively, where α_m is the thermal diffusivity of the melt.

The dimensionless groups appearing in equations (2)–(5) are defined in Table I along with the values of the parameters used in the calculations presented below. The solute diffusivity is D. The definitions of the two Rayleigh numbers follow from expressing the variation of the melt density ρ with temperature and concentration as

$$\rho = \rho_0[1 - \beta_t(T - T_h) + \beta_c(c - c_0)], \tag{6}$$

where ρ_0 is the reference value evaluated at $T = T_h$ and $c = c_0$, and the expansion coefficients are defined as $\beta t \equiv -(1/\rho)(\partial\rho/\partial T)_{\rho,c}$ and $\beta_c \equiv (1/\rho)(\partial\rho/\partial c)_{p,T}$. Positive values of Ra_t correspond to the vertical Bridgman system with melt above solid. Positive values of Ra_s correspond to a solute that increases the density of the alloy. Whether or not this solute stabilizes the melt depends on how it partitions between melt and solid, as determined by the magnitude of the segregation coefficient k. The density profiles corresponding to $k < 1$ are shown in Figure 2 for the cases of $\beta_c < 0$ and $\beta_c > 0$.

The calculations presented in sections 4 and 5 are based on alloys formed by adding solutes to germanium, a well-characterized semiconductor material. For example, silicon partitions preferentially into the solid ($k = 4{\cdot}2$) and is the lighter component in a silicon–germanium alloy. Considering the convectionless solute profile shown in Figure 2 leads to the conclusion that silicon

Table I. Dimensionless groups and their values for calculations representing binary alloys of germanium

Group	Definition	Value
Thermal Rayleigh number	$Ra_t \equiv \beta_t g(T_h - T_c)L^3/\alpha^m\nu$	$0–5 \times 10^6$
Solutal Rayleigh number	$Ra_s \equiv \beta_c g c_0 L^3/\alpha_m\nu$	$0 - \pm 10^6$
Prandtl number	$Pr \equiv \nu/\alpha_m$	0·007
Schmidt number	$Sc \equiv \nu/D$	6·2
Dimensionless growth rate	$Pe \equiv V_g L/\alpha_m$	0·016
Conductivity ratio	$K \equiv k_s/k_m$	1·0
Stefan number	$St \equiv \Delta H_f/\rho_m c_{\rho m}(T_h - T_c)$	4·0
Thermal diffusivity ratio	$\gamma \equiv \alpha_s/\alpha_m$	1·0
Density ratio	$\sigma \equiv \rho_s/\rho_m$	1·0
Ampoule aspect ratio	$\Lambda \equiv R/L$	0·25
Dimensionless length of adiabatic zone	$L_g \equiv \tilde{L}_g/L$	0·25
Segregation coefficient	k	germanium: 0·1 silicon : 4.2
Dimensionless slope of the liquidus line	$m \equiv \tilde{m}c_0/(T_h - T_c)$	silicon : 0·161

should increase the melt density adjacent to the interface; hence it should damp convection in the melt. We also consider a germanium alloy formed with a solute identical to silicon, except that the sign of β_c is reversed so that it destabilizes the melt adjacent to the interface.

The Prandtl and Schmidt numbers are important for the discussion of the numerical results. For a typical metal or semiconductor alloy, the ratio Sc/Pr is extremely high, denoting the large difference between the thermal and species diffusivities in the melt.

The energy equation in the crystal is

$$Pe\,\mathbf{e}_z\cdot\nabla\Theta = \gamma\nabla^2\Theta, \tag{7}$$

where γ is the ratio of thermal diffusivities between the solid and melt and Pe is the dimensionless growth rate; see Table I for definitions.

The location of the melt/solid interface is set by requiring the temperature in each phase to be the alloy melting temperature $\Theta_m(S)$, as determined from the liquidus curve of the binary phase diagram for the material:

$$\Theta_m(r, h(r)) = \Theta_s(r, h(r)) = \Theta_m(S). \tag{8}$$

Balances on heat and species flux at the interface are written as

$$(\mathbf{n}\cdot\nabla\Theta)_m - K(\mathbf{n}\cdot\nabla\Theta)_s = St\,Pe(\mathbf{n}\cdot\mathbf{e}_z), \tag{9}$$

$$(\mathbf{n}\cdot\nabla S)_m = (PeSc/Pr)(\mathbf{n}\cdot\mathbf{e}_z)(1-k)(S+1), \tag{10}$$

where K is the ratio of thermal conductivities between crystal and melt and St is the Stefan number; see Table I. The condition on the concentration field at the inlet which is consistent with the quasi-steady-state model used here is

$$\partial S/\partial z = (PeSc/Pr)S, \tag{11}$$

and is simply a solute balance for melt with incoming concentration $S = 0$.

The boundary conditions on the velocity field along the walls of the ampoule specify no-slip and, along the melt/solid interface,

$$\mathbf{v}\cdot\mathbf{t} = Pe(\mathbf{e}_z\cdot\mathbf{t}), \quad \mathbf{v}\cdot\mathbf{n} = Pe(\mathbf{e}_z\cdot\mathbf{n}), \tag{12}$$

where the first condition is no-slip and the second sets the incorporation of melt into the solid. The centreline of the ampoule is taken to be a line of axial symmetry.

The thermal boundary conditions used in the calculations are shown in Figure 1 and assume that the ampoule has negligible thermal mass and is in perfect thermal contact with the furnace. These assumptions limit the applicability of the results, but are easily removed for accurate modelling of real crystal growth systems.[23]

3. NUMERICAL METHODS

The convection–solidification problem described by equations (2)–(12) is similar to the single-component solidification problem discussed by Chang and Brown,[4] and the basic formulation of the finite element/Newton method follows the approach used there. This technique is reviewed briefly below to highlight the differences needed to incorporate the Petrov–Galerkin formulation, which is discussed in section 3.2.

3.1. Finite element/Newton algorithm

The convection–solidification problem is reduced to a finite-dimensional set of residual

equations by representing the field variables and the interface shape in expansions of Lagrangian basis functions. For an approximate shape of the interface, the melt and solid are discretized into quadrilateral elements, and the field variables are approximated by the mixed finite element set of functions suggested by Huyakorn *et al.*[24] Lagrangian biquadratic polynomials $\{\Phi^i(r,z)\}$, defined on each element, are used to approximate the components of velocity (v_r, v_z), the temperature Θ and solute concentration S fields; and Lagrangian bilinear polynomials $\{\Psi^i(r,z)\}$ are used to approximate the pressure $p(r,z)$. The interface shape $h(r)$ is represented by the set of one-dimensional Lagrangian quadratic polynomials $\{\Phi^i(r)\}$ that is consistent with the isoparametric mapping for a given mesh of elements along the interface. The Petrov–Galerkin formulation of the residual equations is formed by weighting the jth differential equation with the function $W_j^i(r,z)$ and integrating over the appropriate domain. In the Galerkin formulation used by Chang and Brown[4] the weighting functions were chosen to be the basis functions from the respective expansions for the field and interface variables. Here we use the Petrov–Galerkin form

$$W_j^i(r,z) \equiv \Phi^i(r,z) + N_j^i(r,z;\mathbf{v}), \tag{13}$$

where the functions $\{N_j^i(r,z;v)\}$ contain the information about the direction and magnitude of the local velocity field. The form of these extra functions suggested by Heinrich and Zienkiewicz[14] is discussed below. Because the functions $\{N_j^i(r,z;v)\}$ have the same amount of differentiability as the Lagrangian basis functions $\{\Phi_i(r,z)\}$, the development of the algebraic residual equations follows exactly the same approach as that described by Chang and Brown.[4]

The final form of the algebraic equation set is reached by applying the divergence theorem to eliminate second derivatives and by incorporating the boundary conditions on temperature and velocity along the ampoule wall, applying the interfacial energy balance (9), and by forcing the temperature field to be continuous along the interface. The melting point condition, equation (8), is used as the residual equation for the interface shape; residual equations for this one-dimensional equation are formed by weighting it with one-dimensional quadratic basis functions and integrating over the interface. The resulting residual equations are

$$\int_{D_m} \Psi^i(\nabla\cdot\mathbf{v}) r\,dr\,dz = 0, \quad i = 1,\ldots,M, \tag{14a}$$

$$\int_{D_m} [W^i[\mathbf{v}\cdot\nabla\mathbf{v} + \nabla p + Pr(Ra_t(\Theta - 1) - Ra_s S)] + Pr[\nabla W^i\cdot\nabla\mathbf{v}]]\, r\,dr\,dz = 0, \quad i = 1,\ldots,N_m, \tag{14b}$$

$$\int_{D_m} [W^i\mathbf{v}\cdot\nabla\Theta + \nabla W^i\cdot\nabla\Theta]\, r\,dr\,dz - \int_{\partial D_1} W^i StPe(\mathbf{e}_z\cdot\mathbf{n})\,ds = 0, \quad i = 1,\ldots,N_m, \tag{14c}$$

$$\int_{D_m} [W^i(Sc/Pr)\mathbf{v}\cdot\nabla S + \nabla W^i\cdot\nabla S]\, r\,dr\,dz - \int_{\partial D_1} W^i(PeSc/Pr)(\mathbf{e}_z\cdot\mathbf{n})(1-k)(S+1)\,ds - \int_{\partial D_0} W^i(PeSc/Pr)S\,r\,dr = 0, \quad i = 1,\ldots,N_m, \tag{14d}$$

$$\int_{\partial D_s} [W^i Pe(\mathbf{e}_z \cdot \nabla\Theta) + \nabla W^i \cdot \nabla\Theta] r \, dr \, dz = 0, \quad i = 1, \ldots, N_s, \tag{14e}$$

$$\int_{\partial D_l} \phi^i (\Theta - \Theta_m) \, ds = 0, \quad i = 1, \ldots, N_h, \tag{14f}$$

where the notation for the portions of the domain and boundary is shown in Figure 1. The limits on the indices for the residual equations denote the numbers of basis functions in the expansions for the pressure (M), for the components of the biquadratic basis functions for the velocity, temperature and concentration fields in the melt (N_m), for the temperature field in the solid (N_s; excluding the N_h functions defined along the interface), and the number of functions in the one-dimensional expansion for the interface shape (N_h).

The formulation of the weighted residual equations described above assumes that the weighting function W^i is continuous, so that the derivatives are defined. Then the diffusive terms in the equation are modified, as well as the terms representing convection and sources. The weighting functions developed in the streamline/upwinding method of Brooks and Hughes[15] do not have this much continuity, and their application is based on a formulation of the weighted residual equations which does not seem to generalize to quadratic finite element approximations. Another form of the Petrov–Galerkin method for biquadratic approximations to the scalar convection–diffusion equation has recently been proposed by Donea *et al.*[25]

The non-linear set of algebraic residual equations (14) is represented as

$$R(\mathbf{x}; \mathbf{p}) = 0, \tag{15}$$

where $\mathbf{x}$ is the vector of all the unknown coefficients in the expansions for the field variables and the interface shape and $\mathbf{p}$ is the vector of all parameters entering the equation set. Newton's method is used to solve this set in a similar way to that outlined by Chang and Brown.[4]

The two finite element meshes used in the calculations are shown in Figure 3. The coarser mesh (M1) has 8 elements spaced equally across the radius of the ampoule, 16 axial elements in the melt and 8 in the solid. The axial location of each element is connected to the location of the melt/solid interface. The axial spacing of the elements in the melt is graded toward the interface to help approximate the rapid variation in concentration expected there. The finer mesh (M2) has double the number of elements in each direction, as well as radial grading of the elements towards the centreline and the ampoule wall where boundary layers in the solute and velocity fields are expected. The total numbers of non-linear equations generated for each mesh were 2686 (M1) and 10,230 (M2). Execution times for a single Newton iteration on a Cray-1S computer were 11 (M1) and 66 (M2) CPU seconds.

3.2. Petrov–Galerkin formulation for solidification problems

The Petrov–Galerkin weighting functions introduced by Heinrich and Zienkiewicz[14] are based on constructing approximations to the one-dimensional convection–diffusion problem

$$V(dU/dx) - K(d^2U/dx^2) = 0, \quad 0 \leqslant x \leqslant 1, \tag{16a}$$

$$U(0) = U(1) = 0, \tag{16b}$$

which are nodally exact for a solution $U(x)$ represented in Lagrangian quadratic basis functions on a regularly spaced mesh with element size Δ. Then the influence of convection on the numerical approximation is measured in terms of the 'element Peclet Number' $\hat{P} \equiv V\Delta/K$. The extra part of the weighting function in equation (12) is defined for the one dimensional problem as

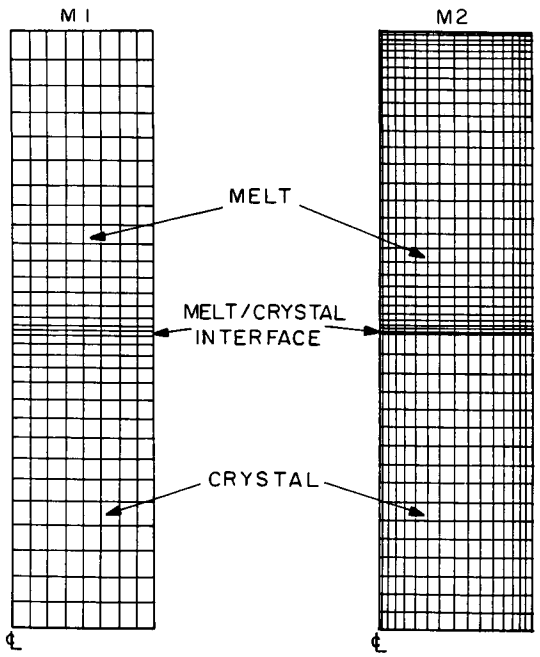

Figure 3. Finite element meshes: (a) M1 and (b) M2

$$N^i(\xi) \equiv -\varepsilon^i(\hat{P})\Gamma(\xi), \quad i = 1, 2, \tag{17}$$

where ξ is the transformed co-ordinate, $-1 \leqslant \xi \leqslant 1$, and the index i differentiates between vertex ($i = 1$) and centroid ($i = 2$) nodes in the Lagrangian quadratic formulation. The modifying function $\Gamma(\xi)$ in equation (17) is the cubic polynomial, $\Gamma(\xi) \equiv (5/8)\xi(\xi - 1)(\xi + 1)$, which vanishes along the boundaries ($\xi = \pm 1$) of the element. Nodally exact values for the solution of equations (16) are obtained by selecting the parameters $\{\varepsilon^i(\hat{P})\}$ to be

$$\varepsilon^{(1)}(\hat{P}) = 2\tanh(\hat{P}/2)[1 + (3/\hat{P})\coth(\hat{P}/4)] - (8/\hat{P}) - \coth(\hat{P}/4), \tag{18a}$$

$$\varepsilon^{(2)}(\hat{P}) = (16/\hat{P}) - 4\coth(\hat{P}/4). \tag{18b}$$

The Petrov–Galerkin weighting functions for the biquadratic basis functions used in our approximations to velocity, temperature and concentration are formed as tensor products of the one-dimensional functions described by equations (17) and (18). In a general flow problem the velocity field is neither unidirectional nor constant within an element, so that the local Peclet number $\hat{P}$ and the weighting coefficients must be computed for each element. A total of twelve upwinding parameters ($\varepsilon_k^{(j)}, j = 1, 2, k = 1, \ldots, 6$) are computed for each two-dimensional element, as shown in Figure 4. The elemental Peclet number is computed for each three-node group as based on the average velocities at the relevant boundary nodes. For example, the value of the elemental Peclet number $\hat{P}$ for the computation of the parameters $\varepsilon_2^{(1)}$ and $\varepsilon_2^{(2)}$ for nodes 4, 5 and 6 (see Figure 4) is approximated as

$$\hat{P} = \frac{(v_{r,8} + v_{r,2})(\Delta r)_{8-2} + (v_{z,8} + v_{z,2})(\Delta z)_{8-2}}{2K}, \tag{19}$$

where Δr and Δz are the linear distances between the nodes 2 and 8, and K is the appropriate diffusivity. Using the linear distances in equation (19) essentially neglects the curvilinear sides of

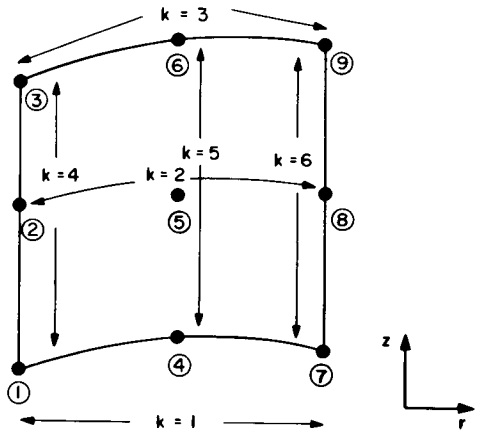

Figure 4. Numbering sequences for application of Petrov–Galerkin weightings to biquadratic isoparametric elements

the general isoparametric elements, but is a good approximation as long as the melt/solid interface is not very deformed. The diffusivities for the dimensionless conservation equations (2)–(4) are unity for the energy equation, Pr/Sc for the solute concentration equation and Pr for the momentum equation.

The Petrov–Galerkin formulation can be incorporated directly into the Newton iteration because the parameters $\{\varepsilon_k^{(j)}\}$ depend explicitly on the finite element approximations for the velocity components at the element nodes and on the location of the nodes (and hence the shape of the melt/solid interface) through the definition of the local Peclet number $\hat{P}$. The needed contributions for the residual equations and Jacobian matrix are computed in closed form. Asymptotic expansions of equations (17) and (18) are used for high ($|\hat{P}| > 25$) and low ($|\hat{P}| < 0{\cdot}1$) values of the Peclet number in order to simplify the calculation.

The Petrov–Galerkin method described above is referred to as P1 and was implemented and tested for calculations with varying growth rates (Pe) and amounts of buoyancy-driven convection (Ra_t); all other parameters were set at the values given in Table I. Although the method gave oscillation-free solute fields (the component of the solution with the smallest diffusivity), the concentration was less accurate than the Galerkin finite element results using the same meshes (M1 and M2). These calculations are described in section 4.

Two test calculations were used to identify the problem with the Petrov–Galerkin formulation P1 as the method of treatment of the mixed boundary conditions for the solute concentration along the inlet and interface. First, calculations with $Ra_t = 0$ and increasing Pe showed the better performance of the conventional Galerkin calculation. In this case, the mixed boundary conditions were the only difference in the computation of the solute field from the problem, equations (17) and (18), for which the Petrov–Galerkin method is exact at the nodes. Secondly, calculations with the same set of residual equations including natural convection, equation (15), but with the essential boundary condition

$$S(r, h(r)) = (1/k) - 1, \quad 0 \leqslant r \leqslant \Lambda, \tag{20}$$

replacing the solute balance, equation (10), showed the superior results for the Petrov–Galerkin method over the Galerkin formulation. The essential boundary condition (20) corresponded to the condition used to derive the weighting functions $\{N_j^{(i)}\}$. The results of these calcuiations also are given in section 4.

Two different remedies were considered to extend the Petrov–Galerkin formulation to the boundary conditions for solidification. New weighting parameters $\{\varepsilon_k^{(j)}\}$ were derived that gave

nodally exact solutions for the one-dimensional solidification problem, but these performed poorly when the flow was cellular and so was not uniaxially aligned with the melt/solid interface. A more fruitful approach resulted from considering the effect of the Petrov–Galerkin method on the interfacial source term in the weak form of the solute balance, equation (14d). Because the modifying function $\Gamma(\xi)$ used to form the Petrov–Galerkin weighting function vanished along all element boundaries, this source term was not changed as the elemental Peclet number increased. We think this caused an imbalance in solute conservation.

We removed the source term from the boundary condition by defining a new concentration variable as the difference between S and the one-dimensional concentration field:

$$S_u(z; h(r)) \equiv \frac{1-k}{k} \exp\left[\frac{PeSc}{Pe}(z - h(r))\right]. \tag{21}$$

In terms of the new concentration variable, $\hat{S} \equiv S - S_u$, the solute balance equation (3) and boundary conditions at the interface (10) and inlet (11) become

$$(Sc/Pr)\mathbf{v}\cdot\nabla(\hat{S} + S_u) = \nabla^2(\hat{S} + S_u), \tag{22}$$

$$(\mathbf{n}\cdot\nabla\hat{S}) = (PeSc/Pr)(\mathbf{e}_z\cdot\mathbf{n})(1-k)\hat{S}, \quad z = h(r), \quad 0 \leqslant r \leqslant 1, \tag{23}$$

$$d\hat{S}/dz = (PeSc/Pr)\hat{S}, \quad z = 0, \quad 0 \leqslant r \leqslant 1. \tag{24}$$

The weighted residual equation (14d) is replaced by the following equation in the new formulation:

$$\begin{aligned}\int_{D_m} [W^i(Sc/Pr)\mathbf{v}\cdot\nabla(\hat{S} + S_u) + \nabla W^i\cdot\nabla(\hat{S} + S_u)]\, r\, dr\, dz \\ - \int_{\partial D_1} W^i(PeSc/Pr)(\mathbf{e}_z\cdot\mathbf{n})(1-k)\hat{S}\, ds \\ + \int_{\partial D_0} W^i(PeSc/Pr)\hat{S}(r,0) r\, dr = 0, \quad i = 1, \ldots, N_m.\end{aligned} \tag{25}$$

New Source terms appear in the area integrals instead of in the boundary integrals; all source terms are influenced by the additional weighting functions. We refer to this formulation as P2. As shown below, this method gives more accurate results for convection-dominated solidification problems than either the P1 Petrov–Galerkin or the Galerkin method.

4. DILUTE BINARY ALLOY: COMPARISON BETWEEEN PETROV–GALERKIN AND GALERKIN METHODS

Calculations were performed with the Galerkin and Petrov–Galerkin formulations for the thermophysical parameters and system configuration listed in Table I. The comparison between the three methods was carried out for calculations describing the solidification of an alloy of dilute gallium in germanium, where the coupling of solute concentration to the density of the alloy was ignored, i.e. $Ra_s = 0$. Then the solute balance equation is decoupled from the momentum and energy equations and reduces to the solution of a scalar convection–diffusion equation with the boundary conditions appropriate for solidification.

Even for mesh M1, the temperature and velocity fields computed with both methods agreed quantitatively for thermal Rayleigh numbers in the range $0 \leqslant Ra_t \leqslant 5 \times 10^6$, and reproduced results discussed by Chang and Brown[5]. Temperature fields computed for this range of Ra_t are shown in Figure 5. In the melt, the temperature decreases from the wall to the centreline for a given

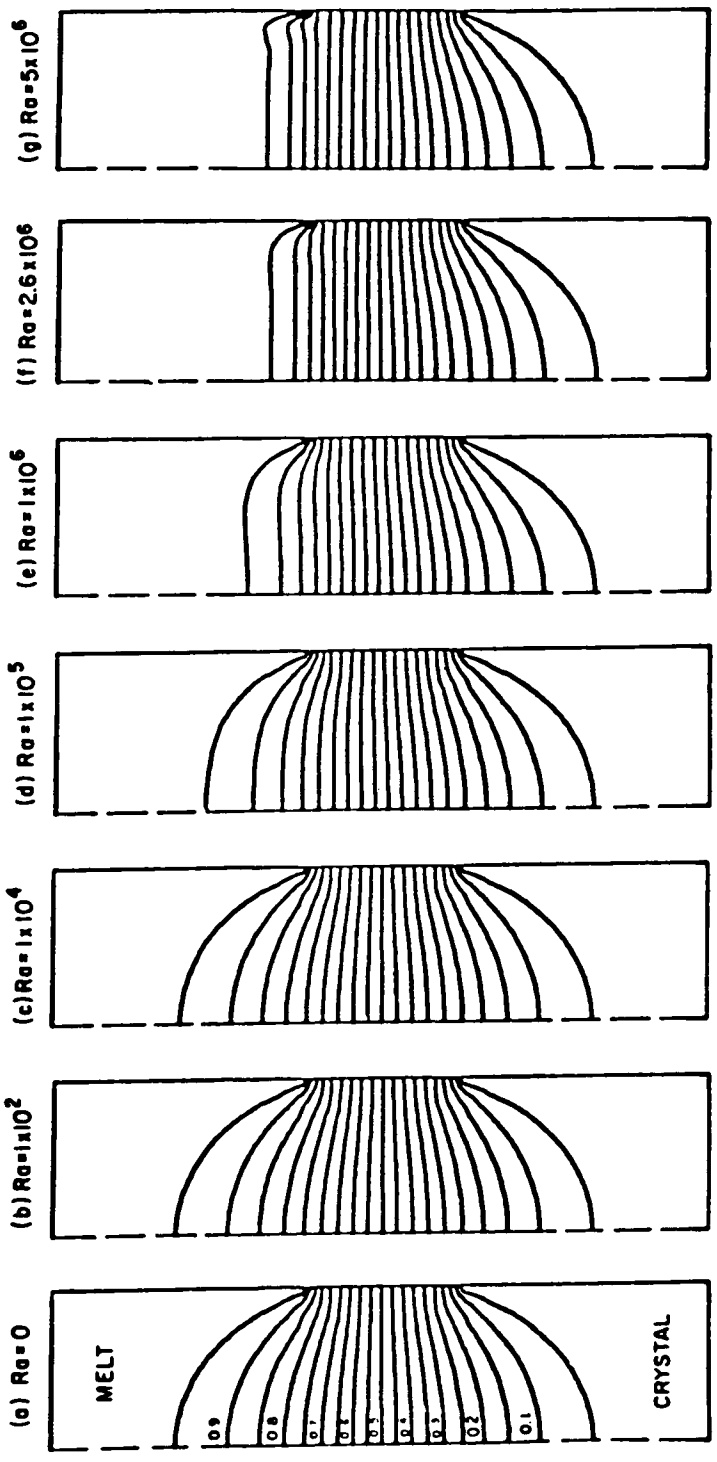

Figure 5. Sample temperature fields for dilute GaGe growth; $0 \leqslant Ra_t \leqslant 5 \times 10^6$. Isotherms are spaced equally at an increment of $\Delta\Theta = 0{\cdot}05$

axial position; the resulting radial temperature gradients are greatest at the junction of the hot and adiabatic zones. The temperature profile is practically symmetric about the melt/solid interface, indicating the negligible effect of latent heat release caused by the crystal growth rate Pe.

The temperature is nearly unchanged for $0 \leqslant Ra_t \leqslant 10^4$ because of the low Prandtl number of the melt. Increasing Ra_t above 10^4 causes the isotherms to compress downward along the axis of the melt and stretch upward at the wall of the ampoule. The interface is deflected little by convection. At $Ra_t = 5 \times 10^6$ the deflection from centreline to ampoule wall is only 6 per cent.

The streamlines shown in Figure 6 correspond to the temperature fields in Figure 5. Three

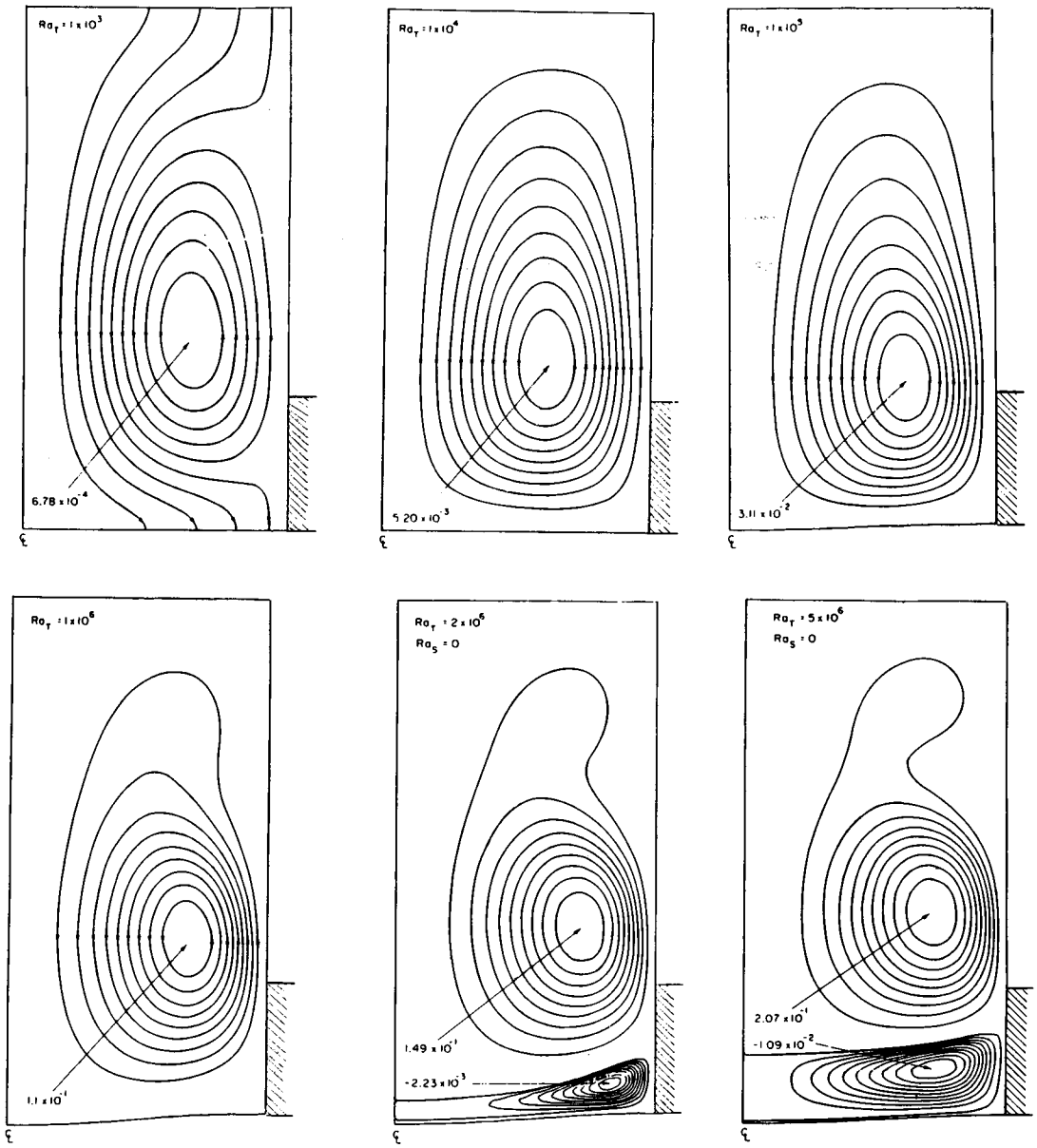

Figure 6. Streamlines for dilute GaGe growth corresponding to the isotherms shown in Figure 5; $0 \leqslant Ra_t \leqslant 5 \times 10^6$

regimes of the flow are evident in this range of Rayleigh numbers. For $Ra_t < 10^3$, the streamlines are essentially those caused by the uniaxial convection due to solidification. A cellular flow developed for $10^3 \leqslant Ra_t \leqslant 10^6$ which moved melt up along the side wall and down along the centreline of the melt. The shape of this cell only changes when the temperature field begins to be influenced by convection. Increasing Ra_t above 10^6 (see Figures 6(e) and 6(f)) caused the formation of a weak secondary cell adjacent to the interface which moved fluid in the opposite sense from the primary cell.

As expected by the large value for the ratio Sc/Pr, the solute field is changed dramatically by far weaker levels of cellular convection, and the accuracy of the solute field is sensitively affected by both the weighted residual method (either Galerkin (G) or Petrov–Galerkin (P1 or P2)) and the mesh. Solute fields computed using Galerkin's method and mesh M1 are shown in Figure 7. For Ra_t as low as 10^3, the solute field is distorted from the one-dimensional exponential profile valid for $Ra_t = 0$. We measure the distortion along the interface in terms of the percentage radial segregation, defined as

$$\Delta c \equiv \left[\max_{0 \leqslant r \leqslant \Lambda} c(r, h(r)) - \min_{0 \leqslant r \leqslant \Lambda} c(r, h(r)) \right] k \times 100 \text{ per cent.} \tag{26}$$

The radial segregation Δc decreases from its near maximum value (63 per cent) at $Ra_t = 10^3$ to 47 per cent at $Ra_t = 10^4$. This decrease is an indication that the solute field is beginning to form a well-mixed core with steep concentration gradients along each boundary of the melt. Galerkin's method cannot capture these layers with mesh M1 and fails abruptly for $Ra_t > 10^4$. The concentration fields computed far larger values of Ra_t have spatial oscillations.

Solute fields computed with the first Petrov–Galerkin method (P1) and mesh M1 are shown in Figure 8. The fields are oscillation-free for Ra_t as large as 10^6. Unfortunately, the accuracy of these fields is much poorer than those computed with Galerkin's method. The first hint of the inaccuracy is the extremely low values of the concentration adjacent to the interface where the expected value is approximately $1/k = 10$.

The global accuracy of approximate solute fields is estimated by computing the average interfacial concentration, defined as

$$\langle c \rangle \equiv \frac{\int_0^{\Lambda} (S+1)(1+h_r^2)^{1/2} r \, dr}{\int_0^{\Lambda} (1+h_r^2)^{1/2} r \, dr}, \tag{27}$$

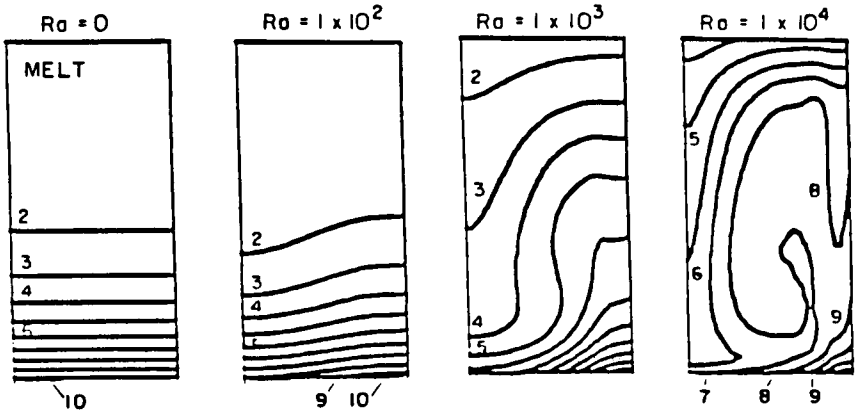

Figure 7. Solute fields computed for dilute GaGe growth using Galerkin's method and mesh M1; $0 \leqslant Ra_t \leqslant 10^4$

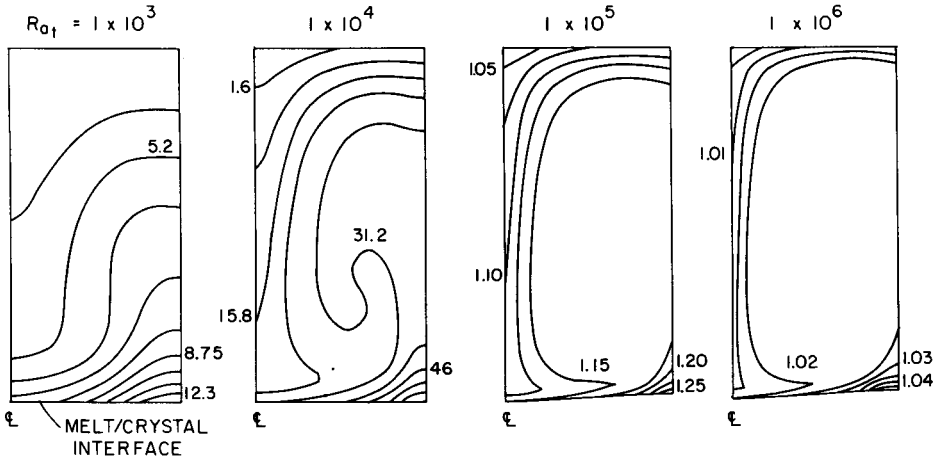

Figure 8. Solute fields computed for dilute GaGe growth using the Petrov–Galerkin method P1 and mesh M1; $10^3 \leqslant Ra_t \leqslant 10^6$

which should be exactly $\langle c \rangle = 1/k$ for the steady-state model. Values of $\langle c \rangle$ computed with the Galerkin and Petrov–Galerkin formulations are listed in Table II. The poor global conservation of solute in the P1 formulation is obvious.

The calculations with the essential boundary condition (20) replacing the solute balance (10) at the interface are shown in Figures 9(a) and 9(b) for the Galerkin (G) and the first Petrov–Galerkin (P1) formulations, respectively. The improvement associated with the Petrov–Galerkin method is clear from the smoothness of the solutions and the values of the concentration near the interface.

Solute fields computed with the second Petrov–Galerkin formulation (P2) are shown in Figure 10 for mesh M1. The fields are smooth and accurate for the same range of Ra_t as Galerkin's method, as indicated by the values of $\langle c \rangle$ listed in Table II. Increasing Ra_t above 10^4 in the P2 formulation results in smooth, but inaccurate solutions. At this point no benefit is obvious from the Petrov–Galerkin method.

Increasing the finite element discretization to mesh M2 showed a clear improvement of the P2 formulation over the Galerkin method, as indicated by the solute fields in Figures 11 (G) and 12 (P2) and the interfacial concentration values given in Table II. Small oscillations developed in the Galerkin calculations for $Ra_t = 10^5$ and became more apparent for $Ra_t = 5 \times 10^5$. The global accuracy of the calculation was destroyed by this convection level.

The results for the P2 formulation with mesh M2 were smooth for Rayleigh numbers up to 2×10^6; see Figure 12. Fairly accurate solutions were computed with the Petrov–Galerkin method up to this value of Ra_t, a significant improvement over the value $Ra_t = 10^5$, beyond which the solute field predicted by Galerkin's method began to oscillate and to yield poor solute balances. It is interesting that the error in $\langle c \rangle$ for the P2 method passes through a maximum with increasing Ra_t. The maximum error in $\langle c \rangle$ seems to correspond to the appearance of the secondary flow cell and the associated maximum in the deflection of the interface shape. The appearance of the secondary cell lowers the magnitude of the velocity adjacent to the boundary, thereby decreasing the steepness of the solute boundary-layer there. Calculations at $Ra_t > 2 \times 10^6$ were less difficult than those where a stronger single flow cell was adjacent to the interface.

Most importantly, the Petrov–Galerkin formulation, when coupled with fine finite element discretizations, allowed calculation of the solute field and the related segregation in the solid through the flow transition from a single-cell to the two-cell flow for $Ra_t > 2 \times 10^6$. This transition

Table II. Interfacial mass balances predicted using Petrov–Galerkin (P1, P2) and Galerkin (G) formulations for $0 \leqslant Ra_t \leqslant 2 \times 10^6$. The exact mass balance is 10·00

Ra_t	Mesh M1			Mesh M2	
	G	P1	P2	G	P2
0	10·00	10·00	10·00	10·00	10·00
10^3	10·11	10·95	10·14	10·00	10·00
10^4	10·21	30·87	10·26	9·91	9·92
10^5	—	1·15	4·26	9·65	9·79
5×10^5	—	—	—	13·21	7·91
10^6	—	—	—	—	7·46
2×10^6	—	—	—	—	9·26

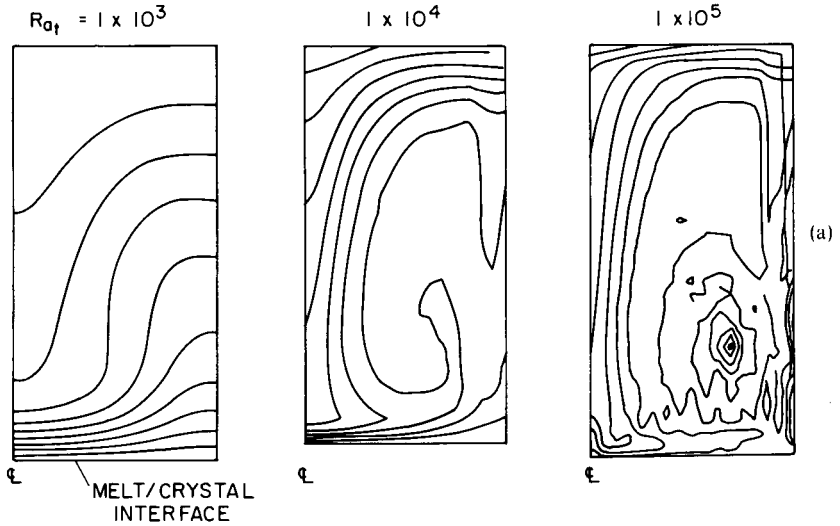

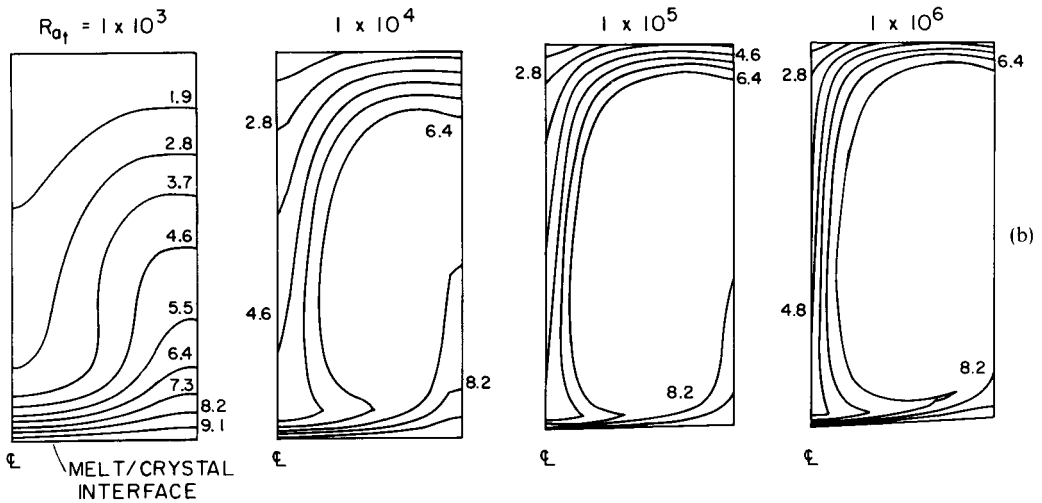

Figure 9. Solute fields computed for dilute GaGe system with the essential boundary condition (20) by both the Galerkin (a) and Petrov–Galerkin (b) (P1) methods: $10^3 \leqslant Ra_t \leqslant 10^6$

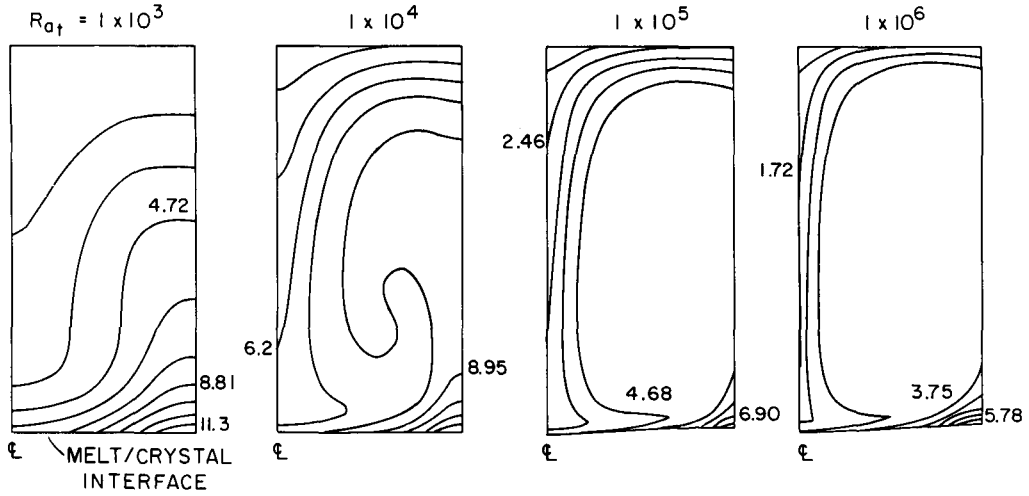

Figure 10. Solute fields computed for dilute GaGe growth with the Petrov–Galerkin method P2 and mesh M1; $10^3 \leqslant Ra_t \leqslant 10^6$

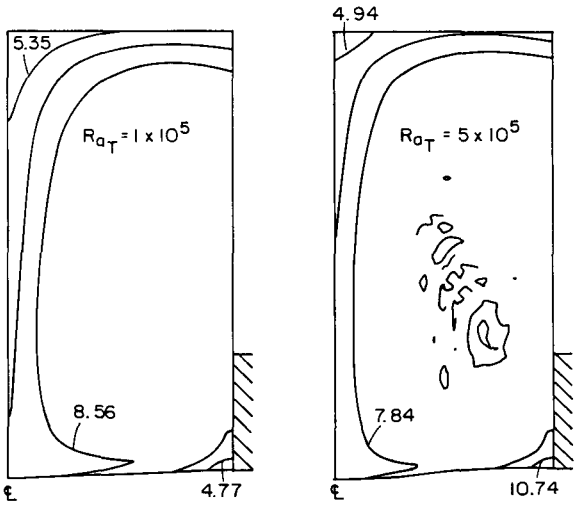

Figure 11. Solute fields computed for dilute GaGe growth using Galerkin method and mesh M2; $10^3 \leqslant Ra_t \leqslant 5 \times 10^5$

is summarized in Figure 13 where the interfacial solute concentrations are plotted across the radius of the solid as a function of Ra_t. The importance of the appearance of the second cell corresponds to an inversion in the location of the maximum concentration along the interface.

5. NON-DILUTE ALLOYS

The Petrov–Galerkin formulation P2 and the finite element mesh M2 were used to study the interactions of convection and interface morphology with the temperature and solute fields for non-dilute alloys. The calculations reported in this section are for an alloy with thermophysical properties similar to the silicon–germanium (SiGe) system, but with the sign of β_c varied to represent both a solutally stabilizing (section 5.1) and a destabilizing (section 5.2) solute. The slope

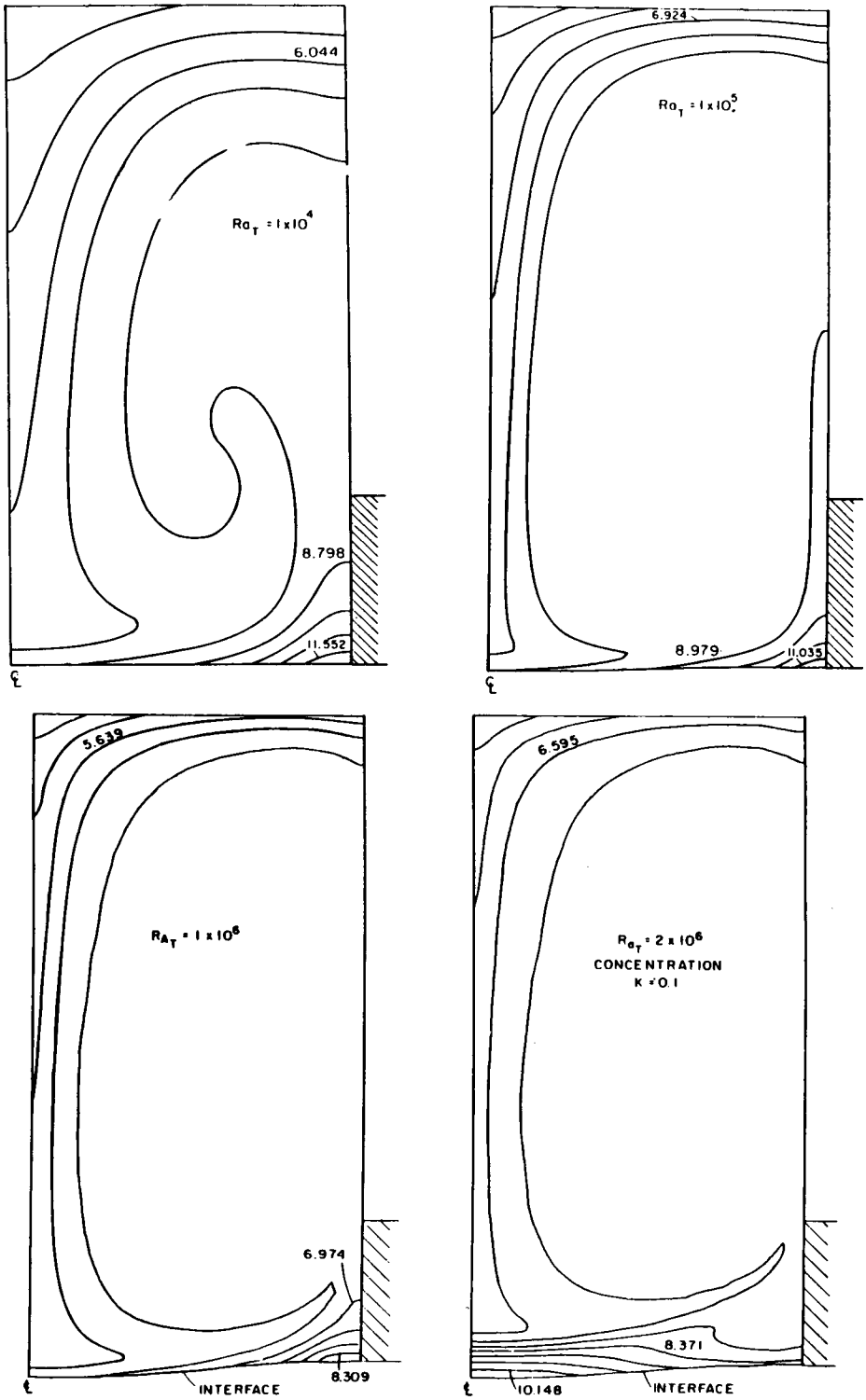

Figure 12. Solute fields computed for dilute GaGe growth with the Petrov–Galerkin method P2 and mesh M2; $10^4 \leqslant Ra_t \leqslant 2 \times 10^6$

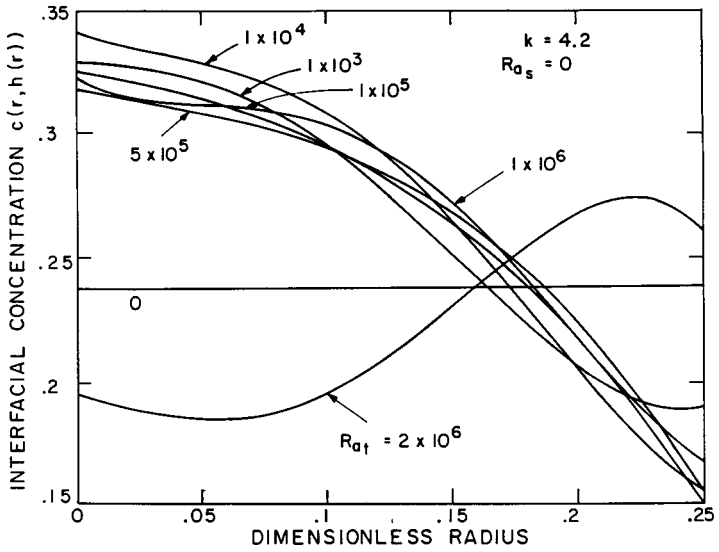

Figure 13. Concentration along the melt/crystal interface as a function of Ra_t for growth of dilute GaGe alloy. Calculations were performed with formulation P2 and mesh M2

of the liquidus curve m is set to zero for the calculations reported in sections 5.1 and 5.2; its effect on the shape of the melt solid interface is examined in section 5.3.

The flow, temperature and concentration fields were computed for a dilute alloy with the segregation coefficient $k = 4.2$ appropriate for the SiGe system as a reference case for the non-dilute calculations. Because the other thermophysical properties were identical with those used for the calculations in section 4, only the solute fields showed any difference from the results displayed in Figures 5 and 6. The solute fields computed with $Ra_s = 0$ are given in Figure 14 for $0 \leqslant Ra_t \leqslant 5 \times 10^6$. The interfacial concentration profiles are shown in Figure 15 and display trends for the location of the maximum and minimum amounts of solute that are opposite to those when the segregation coefficient is less than one. The inversion of the interfacial concentration after the appearance of the secondary flow adjacent to the interface also occurs.

5.1. *Stabilizing alloy:* $Ra_s \leqslant 0$

Introducing a solute that increases the density of the melt adjacent to the interface in large enough concentrations should damp convection. The contours of the stream function, solute concentration and density are shown in Figure 16 for $Ra_s = -10^3$ and $0 \leqslant Ra_t \leqslant 5 \times 10^4$; the temperature fields for these calculations are practically identical to those shown in Figure 5. The dimensionless melt density (ρ/ρ_0) has been computed as

$$(\rho/\rho_0) = [1 - Ra_t(\Theta - 1) + Ra_s(S - 1)](V\alpha_m/gL^3). \tag{28}$$

The solute field is successful at suppressing convection only for thermal Rayleigh numbers below 10^3. The structure of the convection is changed from the cellular flow predicted for the dilute system to almost rectilinear streamlines in the presence of the non-dilute solute. The corresponding radial segregation is $\Delta c = 8{\cdot}9$ per cent in comparison to the value $\Delta c = 58{\cdot}3$ per cent for $Ra_s = 0$.

For higher levels of thermal convection the flow fields are very similar to those for the dilute system shown in Figure 6. At $Ra_t = 5 \times 10^4$, the circulation rate of the flow cell Ψ_{max} is decreased by

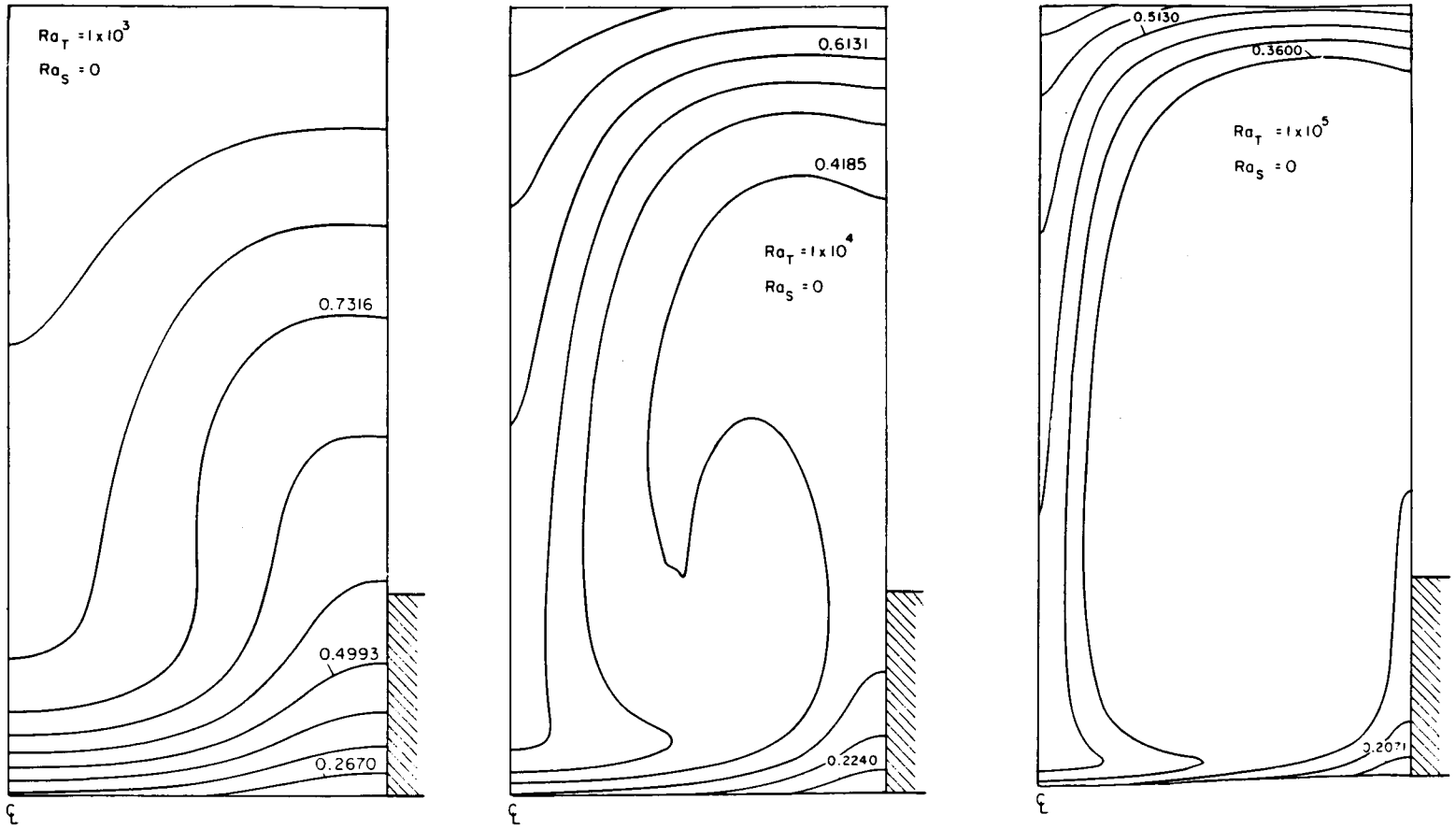

Figure 14. Sample solute fields computed for the dilute silicon–germanium (SiGe) alloy; $Ra_s = 0$ and $10^3 \leqslant Ra_t \leqslant 10^5$

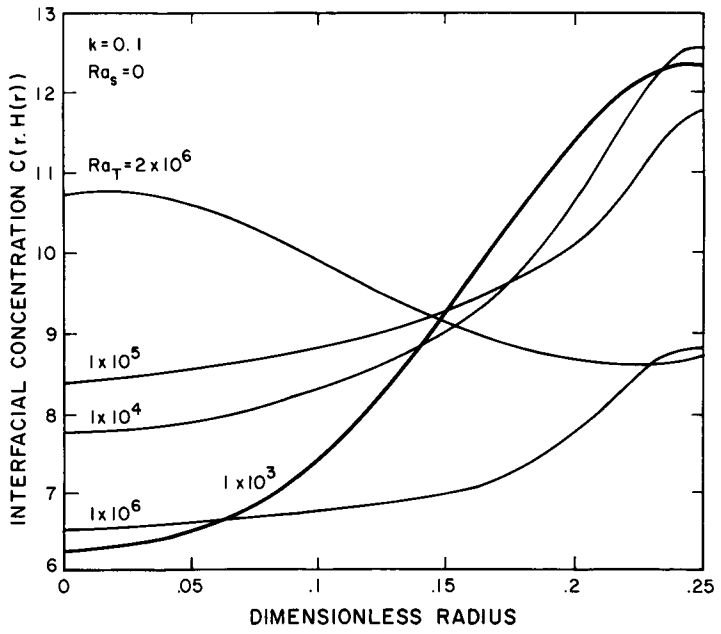

Figure 15. Solute concentration fields along the melt/solid interface for the dilute SiGe alloy as a function of Ra_t

only 0·5 per cent by adding the solute. The large radial variations in the density field near the junction of the adiabatic and hot zones are due entirely to the temperature profile.

Increasing the solutal Rayleigh number to $Ra_s = -5 \times 10^5$ results in almost rectilinear flow and low levels of solute segregation for thermal Rayleigh numbers up to 10^5; see Figure 17. The density in the melt is approximately constant across the radius of the ampoule at each axial location. Calculations at higher values of Ra_s are marked by the appearance of weak flow cells adjacent to the junction of the adiabatic and hot zones; see Figure 17(c). These flows are driven by the steep density gradients in this region caused by the mismatch in the thermal boundary conditions and lead to significant local distortion of the solute field, as shown in Figures 17(b) and 17(c). Because the flows are isolated away from the interface, the concentration profile along it is not disturbed and the amount of radial segregation is less than 5 per cent.

It is interesting that these flows have multiple cells stacked axially above the junction, instead of the single cell seen in the calculations for the dilute alloy, $Ra_s = 0$. The development of the cells in the non-dilute alloy seem to form by the mechanism proposed by Hart[17] for the sideways diffusive instability. Here the flow driven by the slight radial temperature gradient and stabilized by the concentration gradient becomes unstable to the development of axial cells. In the idealized system studied by Hart both the radial temperature gradient and the axial solutal gradient were constant, and the cells developed as a bifurcation from a rectilinear base state. In the vertical Bridgman system, the non-uniform temperature field and exponentially varying axial solute profile are both imperfections to this bifurcation and cause the cells to develop continuously from the basic flow.

Calculations could not be continued for values of Ra_t greater than $4{\cdot}65 \times 10^5$ for $Ra_s = -5 \times 10^5$. The divergence of the Newton iteration for larger values of Ra_t indicated that a limit point appeared in the family of steady-state solutions. We did not implement continuation methods[6] to compute the other solutions expected for lower values of Ra_s because mesh refinement would be needed to guarantee that the limit point is not an artefact of poor

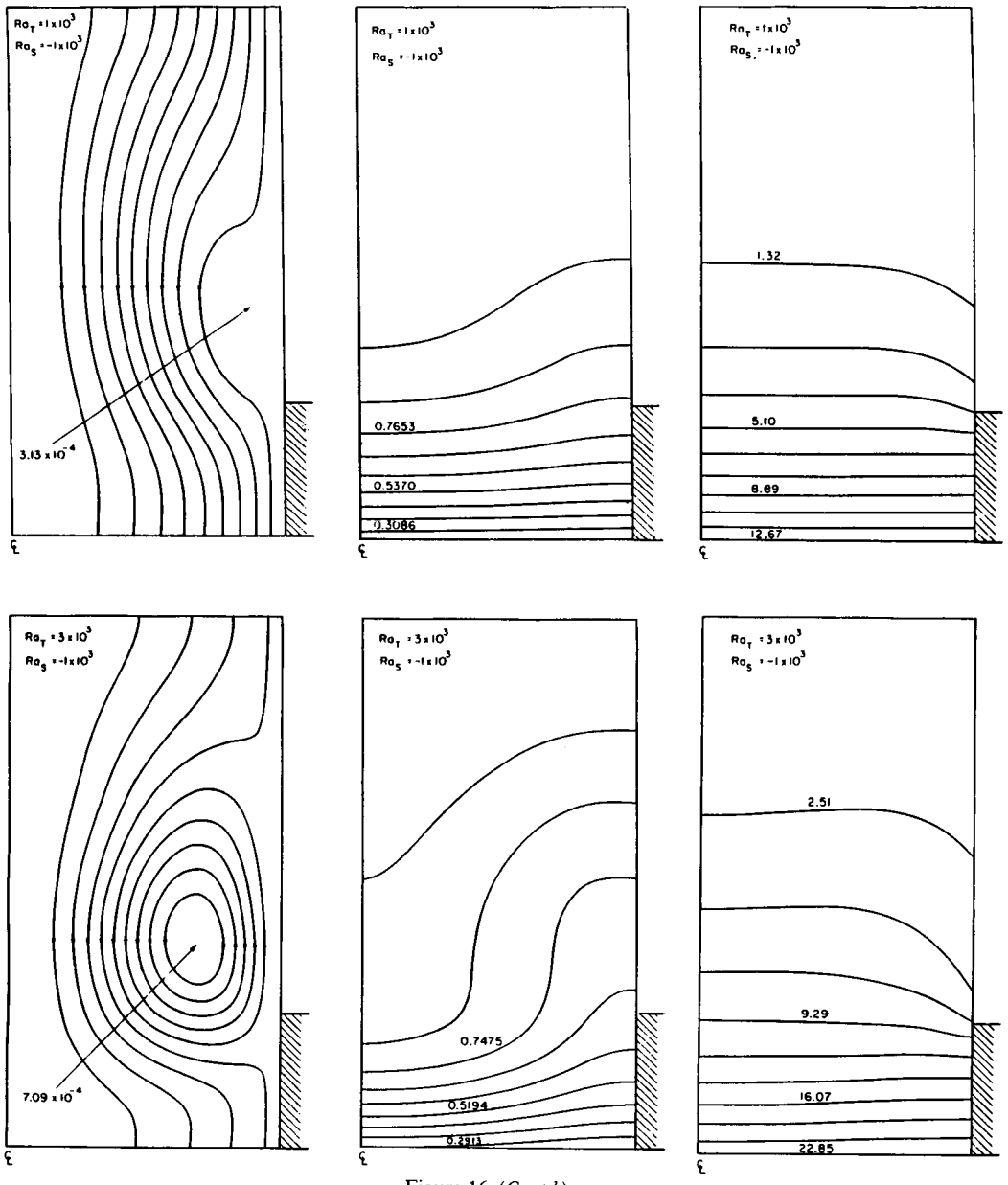

Figure 16. (*Contd.*)

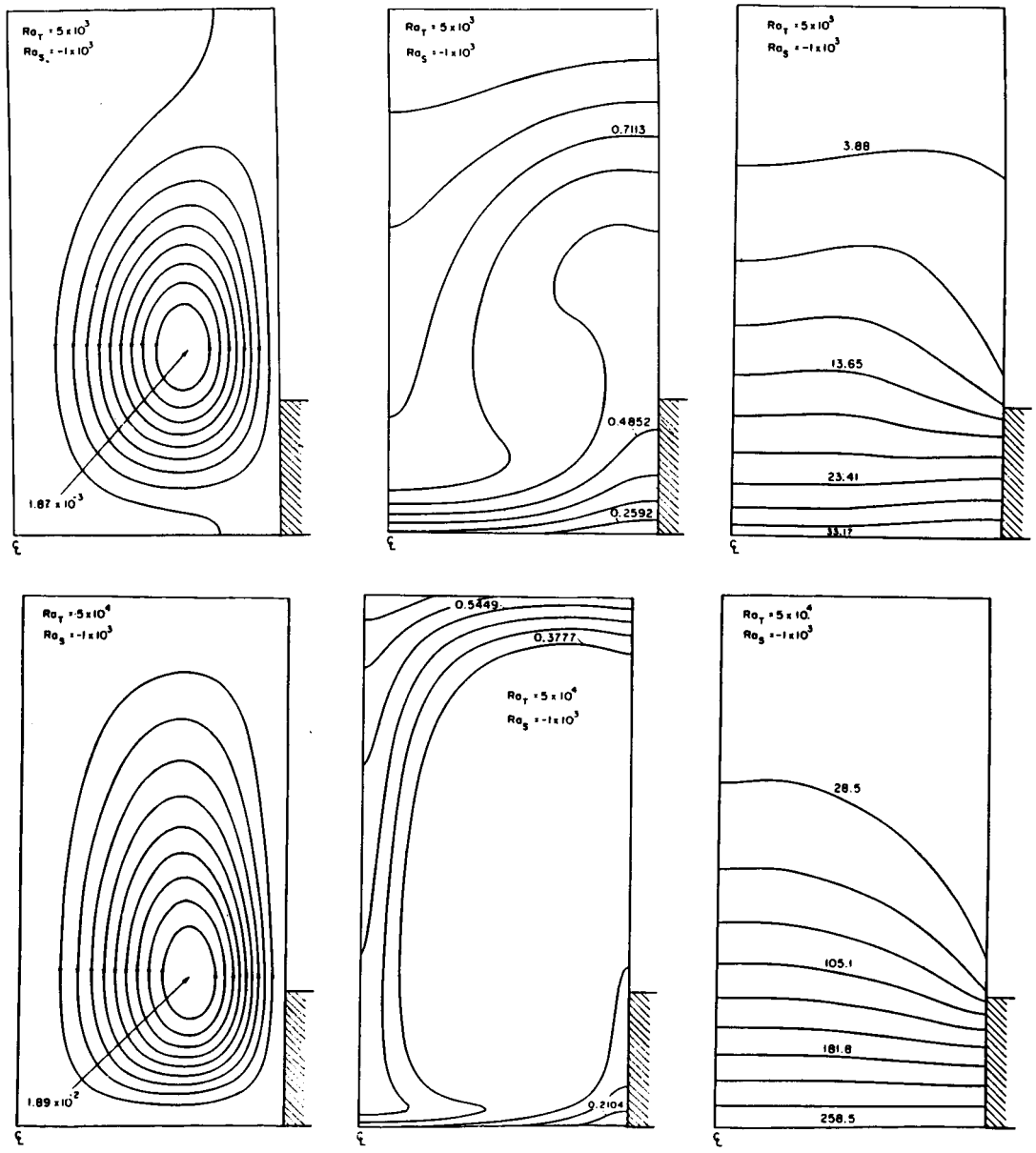

Figure 16. Sample contours of the stream function, solute concentration and melt density for $10^3 \leqslant Ra_t \leqslant 5 \times 10^4$; $Ra_s = -10^3$

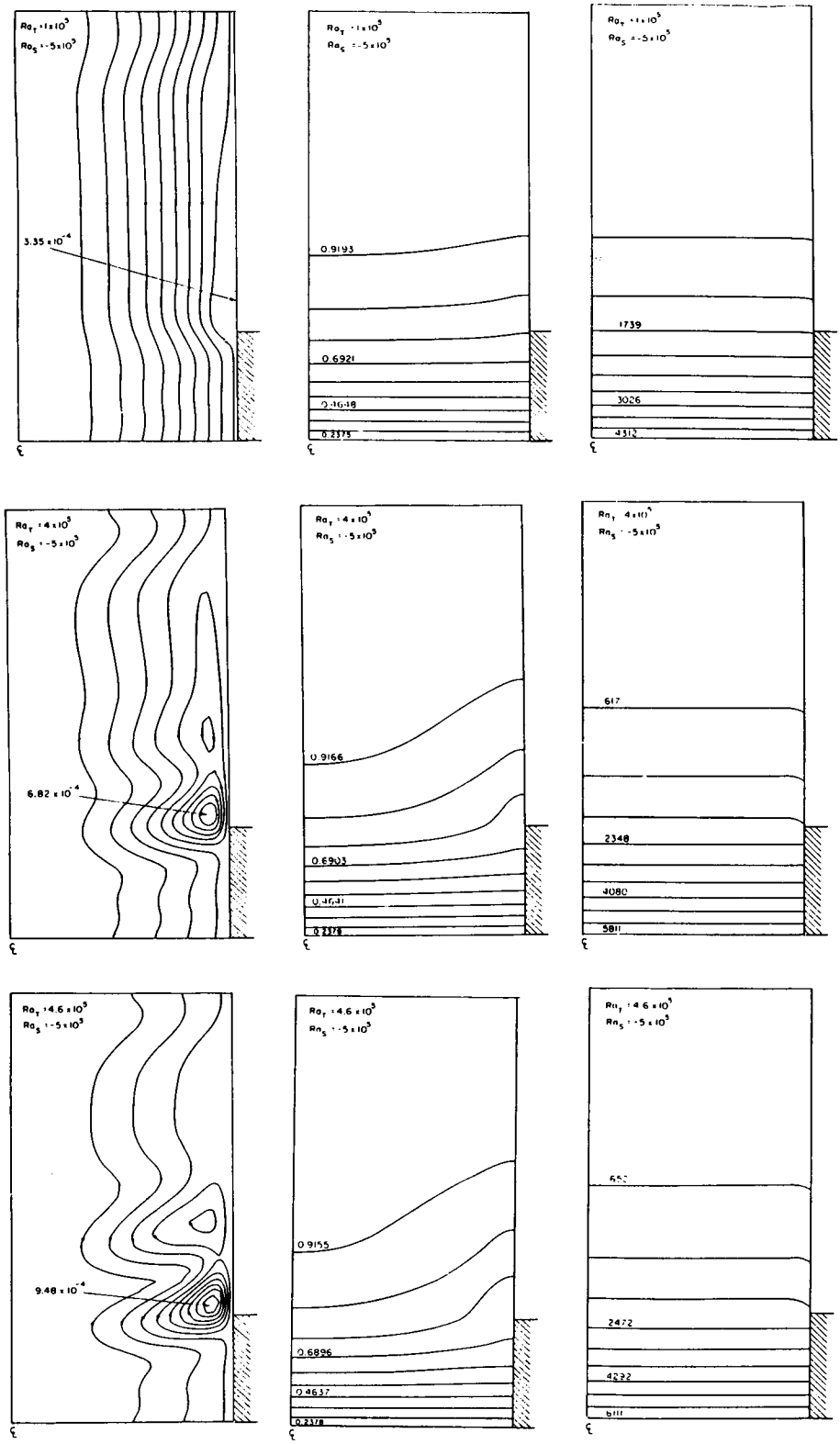

Figure 17. Sample contours of the stream function, solute concentration and melt density for $10^5 \leqslant Ra_t \leqslant 4{\cdot}6 \times 10^5$: $Ra_s = -5 \times 10^5$

approximation to the field variables. A similar limit point has been identified in simulations of thermosolutal convection in a real crystal growth furnace.[23]

Radial segregation along the interface depends more on the magnitude of the thermal convection than on the development of cells by the interaction of the solute and temperature fields. This point is made in Figure 18, where the percentage segregation Δc is plotted as a function of Ra_t for three values of Ra_s. The transition between solutal damping and vigorous thermal convection is evident for $Ra_s = -10^3$. The calculations with $Ra_s = -5 \times 10^5$ terminated before a similar transition could be identified at this higher solute concentration.

5.2. *Destabilizing alloy*: $Ra_s > 0$

Introducing a solute which lowers the density of the melt adjacent to the interface leads to solutally induced convection. McFadden *et al.*[18] studied these flows for a perfectly vertical temperature gradient so that convection begins as a bifurcation from the one-dimensional motion, equation (21). They showed that the bifurcation is supercritical with respect to increasing Ra_s, suggesting that two different flow structures exist for solutal Rayleigh numbers near the critical value. For crystal growth in a cylindrical ampoule these flows will differ by the direction of the circulation in the toroidal cell along the centreline of the ampoule.

The radial temperature gradients inherent to the vertical Bridgman system destroy the symmetry of the one-dimensional state and result in non-uniform convection for any value of Ra_s. The interaction between the thermally induced flows caused by radial gradients is strongest for circulation upward along the ampoule wall. It is expected from simple symmetry arguments that these states compose the family of solutions continuous in Ra_s in the vertical Bridgman geometry. The flows for $Ra_t = 0$ that have circulation down along the ampoule must also still exist, at least for small values of Ra_t, but will be much more distorted by the thermally driven motions. These motions are not connected to the static state $Ra_s = 0$ by a continuous transition in parameters.

We have demonstrated the breaking of the families of solutally driven flows by the radial temperature gradients in calculations for the thermophysical properties of the silicon–germanium alloy, but with a destabilizing solute field, i.e. $Ra_s > 0$. For this system the onset of thermosolutal convection with $Ra_t = 0$ was calculated to occur at $Ra_t^{crit} \simeq 165$ by monitoring the sign of the determinant of the Jacobian matrix evaluated about the one-dimensional solution. Contours of the stream function, solute concentration and dimensionless melt density are shown in Figure 19

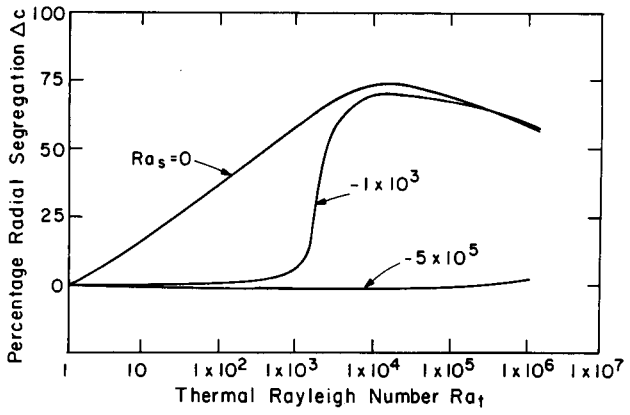

Figure 18. Radial segregation Δc as a function of Ra_t for three values of stabilizing solutal Rayleigh number Ra_s

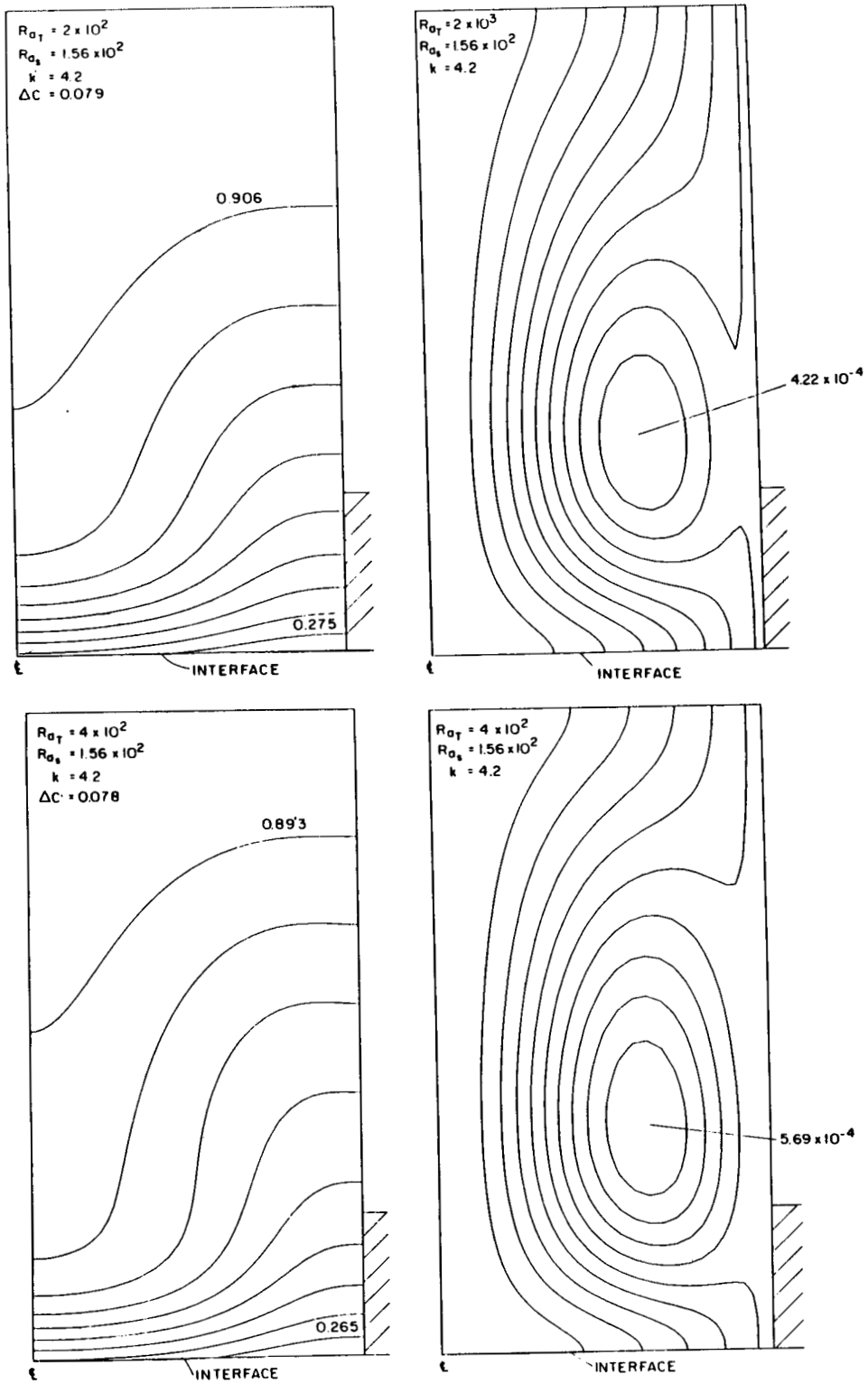

Figure 19. Sample contours of the stream function, solute concentration and melt density for $Ra_t = 200$ and 400 and $Ra_s = 156$

for $Ra_s = 156$, for $Ra_t = 200$ and 400. A weak toroidal cell is predicted near the junction of the adiabatic and hot zones for both values for Ra_t. The density contours for this flow show the internal maximum and minimum characteristic of flows driven by the unstable axial solute gradient, but are distorted by the radial temperature gradients. The counterclockwise motion in the cell has been selected because of the radial temperature gradients. Increasing Ra_s strengthened the circulation and concentrated the unstable solute gradient near the interface. Further increases in either Ra_t or Ra_s stretched the cell to the top of the ampoule.

5.3. *Effect of liquidus slope: onset of morphological instability*

Including the variation of the melting temperature with composition through the phase diagram resulted in larger deflections of the interface and in the possibility of morphological instability.[19] We tested for this by calculations for $m > 0$, with $k = 4{\cdot}2$, $Ra_s = 0$ and $Ra_t = 10^3$. For these conditions material with a higher solute concentration has a higher melting temperature than a more dilute mixture. Concentration fields are shown in Figure 20 with varying m. Including the variation of the melting temperature with concentration pulled the interface up into the melt at the centreline and down near the ampoule wall. These effects are the opposite of the influence of convective heat transport on the interface shape. The maximum interface height appears at the centreline for $m = 0{\cdot}3$; however, the interface has developed aperiodic deflections with a spatial frequency similar to the mesh for $m = 0{\cdot}4$. This qualitative change in interface shape was accompanied by a change in the sign of the determinant of the Jacobian matrix, which indicated the probable loss of temporal stability of the discrete equation set.[6]

We believe that the oscillations in the interface are a numerical instability associated with the onset of morphological instability along the melt/solid interface, which cannot be adequately resolved by either our model for interface shape or by the finite element mesh. For the analysis of a planar interface, neglecting the correction to the melting temperature caused by interface curvature and the surface free energy results in the prediction of morphological instability for all spatial wavelengths, with the fastest growing wavelength being the smallest one. The smallest wavelength that can be resolved by the finite element analysis is set by the size of the elements along the interface. Using the critical wavelength ($\sim 0{\cdot}1R$) appropriate for the mesh M2 and the linear analysis of Mullins and Sekerka[19] for the onset of the instability along a two-dimensional interface yields a critical value of $m \equiv m_c \simeq 0{\cdot}6$. This result agrees reasonably well with the value of the liquidus slope for the onset of the oscillations in the finite element calculations. The theory of Mullins and Sekerka[19] predicts periodic spatial undulations along the interface. The aperiodic shape of the interfaces computed for $m > 0{\cdot}3$ is due to the non-uniform concentration field which acts as an imperfection to the basic instability in the sense described by Chang and Brown.[4] Schaefer and Coriell[26] have observed the non-uniform development of cells in a directional solidification experiment.

6. DISCUSSION

The biquadratic Petrov–Galerkin formulation increased the range of thermosolutal flows which could be computed in steady-state directional solidification problems when used in conjunction with mesh refinement and when the forms of the solidification boundary conditions were taken into account. No advantage of the Petrov–Galerkin (P2) formulation over conventional Galerkin's method was obvious from calculations using a coarse mesh. Although the Petrov–Galerkin solutions were always smooth, the solute concentration fields predicted were grossly inaccurate. The P2 formulation did give significant enhancement of the calculations with the more

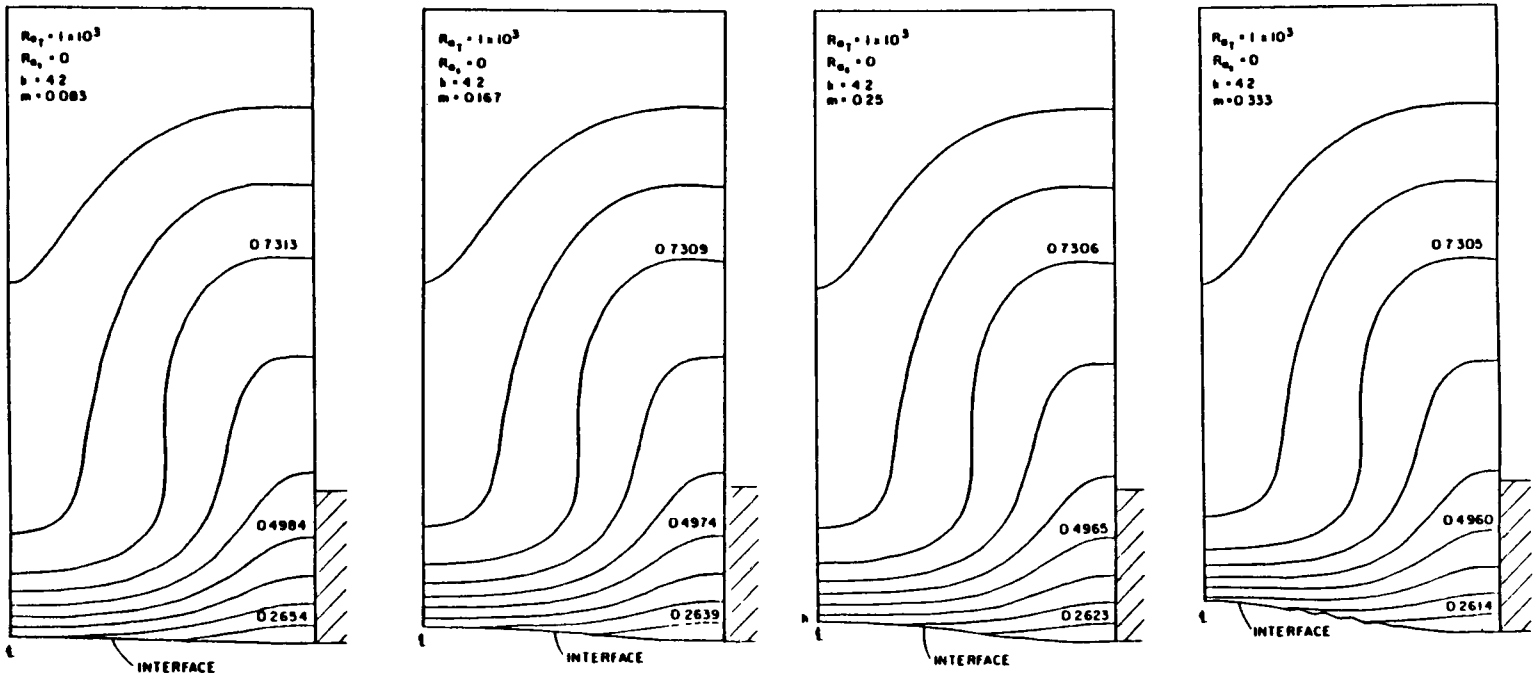

Figure 20. Solute concentration fields computed with varying liquidus slope $m > 0$ and $Ra_t = 10^3$; $Ra_s = 0$ and $k = 4{\cdot}2$

refined mesh M2; globally accurate solute fields were computed for thermal Rayleigh numbers over an order-of-magnitude larger than with the Galerkin method. The increase in the range of thermal Rayleigh number is especially significant, since it allows computations in parameter ranges appropriate for real crystal growth systems.[23] The method is easily implemented in an existing Galerkin finite element code. The change in the weighting function is simply incorporated into the residual equations and into the Newton iteration for solution of the algebraic equation set, thereby leading to an effective algorithm for studying flows, flow transitions and solute segregation in these systems.

The study of the performance of the Petrov–Galerkin method on which these conclusions are based has exposed some of the issues that hinder its general application to a large class of problems. The extra portion of the weighting function vanishes on the boundaries of the element in the formulation used here, so that the Petrov–Galerkin formulation does not affect source terms along the boundary. We found that the overall species balance predicted with the Petrov–Galerkin formulation was in error when these source terms were not taken into account. Altering the form of the equation set to move these source terms into the interior of the domain removed this difficulty; this is the P2 formulation. Neither the streamline/upwinding method of Hughes and Brooks[11] for the bilinear elements nor the new biquadratic Petrov–Galerkin formulation of Donea *et al.*[25] exhibits the loss of accuracy because of the mixed boundary condition, presumably because the weighting functions do not vanish at the boundaries; we elaborate on this point in another paper.

The failure of the P2 method at high convection levels seems to result from under-resolution of the steep gradients associated with the concentration field adjacent to the interface and along the boundaries of the ampoule. Poor approximations to these gradients cause wiggles in the Galerkin formulation and global error in the Petrov–Galerkin results. Only adaptive mesh refinement seems a reasonable cure for this problem in calculations at higher Rayleigh number. The multicellular flows caused by the interactions of the temperature and solute fields result in internal layers and boundary layers in the concentration and temperature fields and point to the extreme complexity of the mesh necessary to capture this structure.

The detection of the morphological instability associated with the coupling of the solute and temperature fields with the interface shape is only one example of the interesting instabilities that arise in systems with convection and solidification; see Reference 27 for others. The appearance of undulations along the melt/solid interface as a numerical instability demonstrates the difficulty associated with solution of a transport problem with extremely disparate length scales. Improvements are needed in the accuracy and efficiency of large-scale calculations before such problems can be solved effectively.

ACKNOWLEDGEMENTS

This research was supported by the Microgravity Sciences Program of the U.S. National Aeronautics and Space Administration and by a grant from the U.S. Department of Energy for use of the computer facilities at the Los Alamos National Scientific Laboratory.

REFERENCES

1. W. E. Langlois, 'Buoyancy-driven flows in crystal-growth melts', *Ann. Rev. Fluid Mech.*, **17**, 191–215 (1985).
2. R. A. Brown, 'Modelling of convection and solidification in melt crystal growth', in P. Dryburgh (ed.), *Advanced Crystal Growth*, North-Holland, in press, 1987.
3. C. J. Chang and R. A. Brown, 'Finite element methods for buoyancy-driven convection near melt/solid phase boundary', in T. Shih (ed.), *Numerical Methodologies in Heat Transfer;* Hemisphere Press, 1983 pp. 283–304.
4. C. J. Chang and R. A. Brown, 'Natural convection in steady solidification: finite element analysis of a two-phase Rayleigh–Benard problem', *J. Comput. Physics*, **53**, 1–27 (1984).

5. C. J. Chang and R. A. Brown, 'Radial segregation induced by natural convection and melt/solid interface shape in vertical Bridgman growth', *J. Crystal Growth*, **63**, 343–364 (1983).
6. Y. Yamaguchi, C. J. Chang and R. A. Brown, 'Multiple buoyancy-driven flows in a cylinder heated from below', *Philos. Trans. Roy. Soc. Lond.*, **312**, 519–552 (1984).
7. C. A. Wang, 'Crystal growth and segregation in vertical Bridgman configuration', *Ph.D. Thesis*, Massachusetts Institute of Technology, 1984.
8. P. M. Gresho and R. L. Lee, 'Don't suppress the wiggles—they're telling you something!', in T. J. R. Hughes (ed.), *Finite Element Methods for Convection-Dominated Flows, AMD Vol. 34*, ASME, New York, 1979.
9. B. P. Leonard, 'A survey of finite differences of opinion on numerical muddling of the incompressible defective confusion equation', in T. J. R. Hughes (ed.), *Finite Element Methods for Convection-Dominated Flows, AMD Vol. 34*, ASME, New York, 1979.
10. T. J. R. Hughes, 'A simple scheme for developing upwind finite elements', *Int. j. numer. methods eng.*, **12**, 1359–1365 (1978).
11. T. J. R. Hughes and A. Brooks, 'A theoretical framework for Petrov–Galerkin methods with discontinuous weighting functions: application to the streamline-upwind procedure', in R. H. Gallagher (ed.), *Finite Element in Fluids, Vol. 4*, Wiley, New York, 1982.
12. D. W. Kelly, S. Nakazawa, O. C. Zienkiewicz and J. C. Heinrich, 'A note on upwinding and anisotropic balancing dissipation in finite element approximations to convective diffusion problems', *Int. j. numer. methods eng.*, **15**, 1705–1711 (1980).
13. I. Christie, D. F. Griffiths, A. R. Mitchell and O. C. Zienkiewicz, 'Finite element methods for second-order differential equations with significant first derivatives', *Int. j. numer. methods eng.*, **10**, 1389–1396 (1976).
14. J. C. Heinrich and O. C. Zienkiewicz, 'Quadratic finite element schemes for two-dimensional convective transport problems', *Int. j. numer. methods eng.*, **11**, 1831–1844 (1977).
15. A. Brooks and T. J. R. Hughes, 'Streamline upwind/Petrov–Galerkin formulation for convection dominated flows with particular emphasis on the incompressible Navier–Stokes equations', *Comp. Meth. Appl. Mech. Eng.*, **32**, 199–259 (1982).
16. J. C. Heinrich, 'A finite element model for double diffusive convection', *Int. j. numer. methods eng.*, **20**, 447–464 (1984).
17. J. E. Hart, 'On sideways diffusive instability', *J. Fluid Mech.*, **49**, 279–288 (1971).
18. G. B. McFadden, R. G. Rehm, S. R. Coriell, W. Chuck and K. A. Morrish, 'Thermosolutal convection during directional solidification', *Metall. Trans.*, **A15**, 2125–2137 (1984).
19. W. W. Mullins and R. F. Sekerka, 'Stability of a planar interface during solidification of a dilute binary alloy', *J. Appl. Physics*, **35**, 444–451 (1964).
20. L. H. Ungar and R. A. Brown, 'Cellular interface morphologies in directional solidification. 1. The one-sided model', *Physical Review*, **B29**, 1367–1380 (1984).
21. L. H. Ungar and R. A. Brown, 'Cellular interface morphologies in directional solidification. 2. The effect of grain boundaries', *Physics Review*, **B30**, 3993–3999 (1984).
22. M. C. Flemings, *Solidification Processing*, McGraw-Hill, New York, 1974.
23. P. M. Adornato and R. A. Brown, 'The effect of ampoule on convection and segregation during vertical Bridgman growth of dilute and non-dilute binary alloys', *J. Crystal Growth*, **80**, 155–190 (1987).
24. P. S. Huyakorn, C. Taylor, R. L. Lee and P. M. Gresho, 'A comparison of various mixed-interpolation finite elements in the velocity-pressure formulation of the Navier–Stokes equations', *Computers and Fluids*, **6**, 25–35 (1978).
25. J. Donea, Belytschko and P. Smolinski, 'A generalized Galerkin method for steady convection-diffusion problems with application to quadratic shape function elements', *Comp. Meth. Appl. Mech. Eng.*, **48**, 25–43 (1985).
26. R. J. Schaefer and S. R. Coriell, 'Convection-induced distortion of a solid–liquid interface', *Metall. Trans.*, **A15**, 2109–2115 (1984).
27. M. E. Glicksman, S. R. Coriell and G. B. McFadden, 'Interaction of flows with crystal-melt interface', *Ann. Rev. Fluid Mech.*, **18**, 307–335 (1986).